

THESIS FOR THE DEGREE OF LICENTIATE OF ENGINEERING

Vibrational energy harvesting for sensors in vehicles

JOHAN BJURSTRÖM

Department of Microtechnology and Nanoscience

CHALMERS UNIVERSITY OF TECHNOLOGY

Gothenburg, Sweden 2022

Vibrational energy harvesting for sensors in vehicles

JOHAN BJURSTRÖM

© JOHAN BJURSTRÖM, 2022.

Chalmers University of Technology
Microtechnology and Nanoscience - MC2
SE-412 96 Göteborg, Sweden
Telephone + 46 (0)31-772 1000

ISSN 1652-0769
Technical report MC2-459

Abstract

The miniaturization of semiconductor technology and reduction in power requirements have begun to enable wireless self-sufficient devices, powered by ambient energy. To date the primary application lies in generating and transmitting sensory data. The number of sensors and their applications in automotive vehicles has grown drastically in the last decade, a trend that seems to continue still. Wireless self-powered sensors can facilitate current sensor systems by removing the need for cabling and may enable additional applications. These systems have the potential to provide new avenues of optimization in safety and performance.

This thesis delves into the topic of vibrations as ambient energy source, primarily for sensors in automotive vehicles. The transduction of small amounts of vibrational, or kinetic, energy to electrical power, also known as vibrational energy harvesting, is an extensive field of research with a plethora of inventions. A short review is given for energy harvesters, in an automotive context, utilizing transduction through either the piezoelectric effect or magnetic induction. Two practical examples, for ambient vibration harvesting in vehicles, are described in more detail. The first is a piezoelectric beam for powering a strain sensor on the engines rotating flexplate. It makes combined use of centrifugal force, gravitational pull and random vibrations to enhance performance and reduce required system size. The simulated power output is 370 μW at a rotation frequency of 10.5 Hz, with a bandwidth of 2.44 Hz. The second example is an energy harvesting unit placed on a belt buckle. It implements magnetic induction by the novel concept of a spring balance air gap of a magnetic circuit, to efficiently harvest minute vibrations. Simulations show the potential to achieve 52 μW under normal road conditions driving at 70 km/h.

Theoretical modeling of these systems is also addressed. Fundamental descriptions of the lumped and distributed models are given. Based on the lumped models of the piezoelectric energy harvester (PEH) and the electromagnetic energy harvester (EMEH), a unified model is described and analyzed. New insights are gained regarding the pros and cons of the two types of energy harvester run at either resonance or anti-resonance. A numerical solution is given for the exact boundary of dimensionless quality factor and dimensionless intrinsic resistance, at which the system begins to exhibit anti-resonance. Regarding the maximum achievable power, the typical PEH is favored when running the system in anti-resonance and the typical EMEH is favored at resonance. The described modeling considers all parameters of the lumped model and thus provides a useful tool for developing vibrational energy harvester prototypes.

Keywords: vibration energy harvesting, unified modeling, piezoelectric, electromagnetic induction, anti-resonance, prescribed displacement, automotive safety, low frequency, small amplitude excitation, nonlinear dynamics

List of publications

Paper I

J. Bjurström, F. Ohlsson, A. Vikerfors, C. Rusu and C. Johansson

“Tunable spring balanced magnetic energy harvester for low frequencies and small displacements”

Energy Conversion and Management 259 (2022) 115568

Paper II

J. Bjurström, F. Ohlsson, C. Rusu and C. Johansson

“Unified modeling and analysis of vibration energy harvesters under inertial loads and prescribed displacements”

Applied Sciences 2022, 12, 9815

Acknowledgements

The list is long, of those deserving of acknowledgment, and gratitude, for bringing me to this point. From the very beginning the people in our lives affect its direction and are inevitably a part of how we wind up where we are now. I cannot mention you all here but know that I am grateful.

This thesis work I owe to my supervisor Cristina Rusu, who invited me into this field of research. Thank you for making my PhD experience as positive as possible, with the best possible outcome, and thank you for your warm-hearted mentorship and wise guidance.

I am thankful for Per Lundgren and Peter Enoksson and their support and valuable advice.

I am also very thankful for Christer Johansson and Fredrik Ohlsson and their enthusiasm in sharing their wealth of knowledge and discussing ideas.

I am grateful for The Swedish Foundation for Strategic Research (project FID16-0055), Chalmers and RISE for providing the means for me to perform my research. Also, I am thankful to Autoliv for this interesting and very challenging research topic opportunity and ReVibe for inspiring electromagnetic discussions.

The greatest debt of gratitude of course goes to my family, for they have shared in my troubles with none of the gain.

To my father for his useful input in scientific discussions and instilling me with the essence of the scientific process.

To my mother for her empathy and for always listening.

To my sister for being the best of role models and always waiting with open arms.

To my son for making me laugh in the darkest of times.

To my wife for being an inspiration in life and driving me to grow. For her wisdom and emotional support throughout it all. For her love and the joy it gives me.

Mölndal, November 2022

Johan Bjurström

Abstract	I
List of publications.....	III
Acknowledgements	V
1.1 Introduction.....	1
1.2 Vibrational energy harvesting in vehicles	2
1.3 Vibrational energy harvester system	5
1.3.1 Transduction mechanisms.....	6
1.4 Optimization of power output	7
1.4.1 Resonance and anti-resonance	8
1.4.2 Stochastic resonance	9
1.4.3 Impedance matching	9
1.5 Scope	10
2.1 Introduction to piezoelectricity.....	11
2.2 Piezoelectric energy harvester research	13
2.3 Piezoelectric energy harvester for engine sensor	15
3.1 Introduction to electromagnetic induction.....	21
3.2 Research in electromagnetic energy harvesting	22
3.3 Electromagnetic energy harvester for safety sensor in belt buckle.....	23
4.1 Introduction to modelling of vibration energy harvesters.....	31
4.2 Analysis of a unified model for vibration energy harvetsters	33
5.1 Discussion and concluding remarks	41
5.2 Future work	42
References	43
Publications	51

1.1 Introduction

Energy harvesters (EH's) refers to the small-scale technology for converting ambient energy to a useful form. In modern society the most useful form is typically electrical energy. A common source of ambient energy is movement, i.e., kinetic energy, for example from moving or vibrating parts in devices or vehicles. A vibrational energy harvester (VEH) is a small device for scavenging ambient kinetic energy and converting it to electrical energy. State-of-the-art VEH range in size from centimeters to nanometers and generate electrical power in the range of nano watts to watts, depending on their purpose and environment.

The very first instance of kinetic energy harvesting dates to the early 1800s [1,2] and the invention of the electrical generator by Michael Faraday (Figure 1 left), utilizing magnetic induction. At this time Faradays invention was a simple and safe way of generating small amounts of electricity for use in scientific research but evolved to grow in scale and become the main means with which we generate electricity throughout society. Additional methods for generating electricity from movement were demonstrated in the late 1800s and early 1900s but were impractical to scale in size to produce commercially useful amounts of electrical power. Until the 21st century there was no commercial incentive in small-scale energy harvesting devices. However, this fact began to change by the introduction of semiconductor technology and in extension processor units.

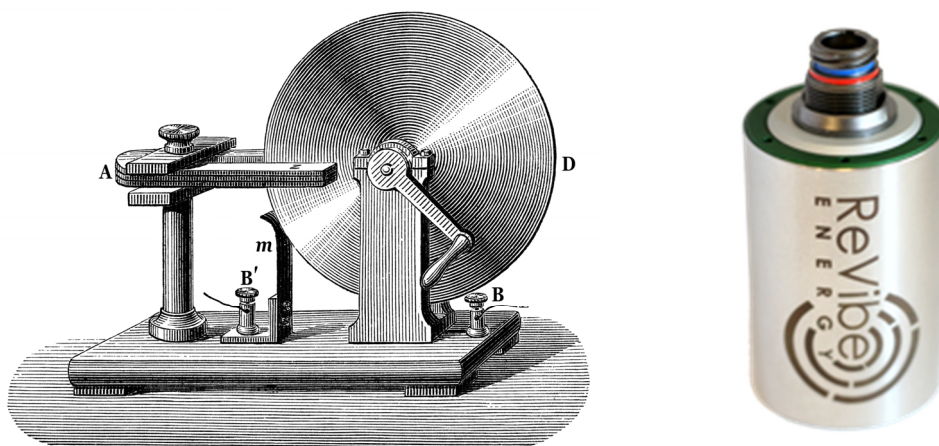


Figure 1. Left: A depiction of Faradays original electric generator [3]. Right: A modern commercial electromagnetic energy harvester.

The advancements in semiconductor technology have resulted in commercially available ultra-low power microprocessors ($<100\text{ }\mu\text{W}$ [4]) and transceivers with average power consumption below 1 mW and as low as $267\text{ }\mu\text{W}$ for rudimentary transmission (as reported in research [5–8]). Since the beginning of the 21st century [9] research in vibrational energy harvesting has been increasing the energy conversion efficiency and power density (size relative power output) of energy harvesting devices. We are now at a point where state-of-the-art VEH can produce electrical power in the same magnitude as the power consumption of some processors and transceivers. Using energy harvesting for powering commercial small-scale applications is now a reality and with continued progress in research the number of viable applications will grow.

1.2 Vibrational energy harvesting in vehicles

The most evident benefit of energy harvesting is self-sustained electronics for cases where access is difficult or impossible and in cases where many units result in high maintenance costs or cumbersome power cabling. An important area where self-sustained electronics can be beneficial is in automotive applications [10–12], primarily considering sensors for safety and performance optimization. An automotive vehicle has a number energy sources which may be exploited by energy harvesting in general, such as heat, RF-signals and sunlight. Within a vehicle, these are however limited in region or availability [13]. Significant kinetic energy, in the form of vibrations, is available throughout the vehicle.

The current trend in the development of automotive vehicles is an increased use of sensors and computational power (see Figure 2 for examples of sensors in cars). Some examples are adaptive power train control for increased efficiency [14,15], tire pressure sensing, tire grip indicators, and safety systems such as “Lane assist”, “early obstruction detection”, “Driver alertness” and “air bag control”. All these systems rely on sensory input, leading to an increasing number of sensors. Increasingly autonomous vehicles also create an increased reliance on sensory input, enabling the onboard machine learning algorithms to reach their full potential.

Integration of a large number of sensors is challenging to realize if batteries must be utilized (due to replacement need, inaccessible deployment, large quantities and environmental impact). Alternatively, wired power distribution is needed, increasing weight/cost and complicating the installation due to limited space. Most sensors require a low power input, in a range close the capabilities of state-of-the-art VEH given the typical vibrational environment of modern vehicles. The most promising solution is therefore self-powered sensor systems. In this way, it reduces the weight and saves cost by reducing the amount of cables in the car without reducing the robustness of the system, allowing to increase the number of sensors in the car, reduce risks and increase safety.

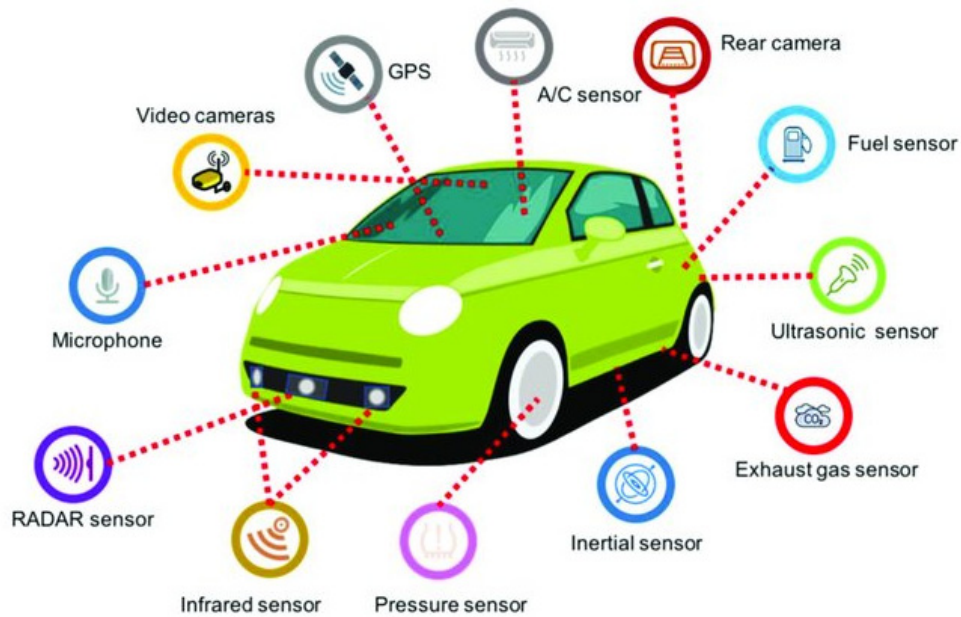


Figure 2. Modern automotive vehicle sensor applications [16].

Much of the research for VEH's in vehicles is focused on areas where there is a large amount of available energy. These areas are primarily the vehicle suspension [17], wheel rotation [18] and on-engine vibrations [19–21].

VEH drawing power from the vehicles suspension system are typically based on an electromechanical transduction element placed in parallel with the vehicles shock absorbers. A review of the various designs implemented in this regard is given by Abdelkareem et al. (2008 [17]). Zhao et al. (2019 [22]) describe a system where the parallel electrical damping is achieved by a piezoceramic cylinder connected via a lever with variable pivot point. This design allows the force transmitted to the piezoceramic to be adjusted. The average measured power was 18 W driving at 60 km/h. Zhao et al. (2019 [23]) and Alhumaid et al. (2022 [24]) implement motion conversion from axial to rotation together with varying magnetic force exerted on piezoelectric elements. Zhao et al. test their system under real road condition, measuring an average power of 332 W driving at 120 km/h. The VEH by Alhumaid et al. generates only 0.95 mW but is only tested in lab conditions with a small vibration frequency and amplitude. An axisymmetric cylindric EMEH for suspension damping is implemented by Zhou et al. (2022 [25]). It uses a stack of two magnets moving within a stack of coils. Iron components are added to guide the magnetic flux and increase the magnetic field gradients within the coils. The EMEH generates 340 mW at 3.3 Hz with a displacement amplitude of 2 mm.

VEH's in tires can scavenge energy from one or a combination of sources, such as tire deformation, the alternating relative direction of gravitational pull and road vibrations. A strain based PEH, embedded on the inner surface of the tire, is described by Esmaeeli et al. (2019 [26]) and they state their VEH generates 24 μ J per revolution. Seo et al. (2019 [27]) implements an EMEH with nonlinear magnetic springs, placed vertically aligned on the inner surface of the tire, scavenging energy from impacts and vibration. The lab-based measurements showed a power output of 5.7 mW at 60 km/h. An EMEH converting the wheel

rotational energy through a plucking mechanism, developed by Miao et al. (2022 [28]), generates an average power of 13 mW at approx. 20km/h.

The power output from PEH externally placed on some surface of the engine has a significant dependance of the engine rpm [19–21]. Gao et al. (2017 [19]) implement a rod with seismic mass to induce strain in a stack of piezo discs, which generates 30 μ W under lab conditions (at 60Hz and 1g acceleration) and 0.4 μ W on engine (after engine has achieved a stable state). To increase the bandwidth, Koo et al. (2021 [20]) use a double cantilever PEH, which delivers 0.181 mW under lab-conditions with 1 g excitation corresponding to running an engine at 2200 rpm. The corresponding field measurement shows only 0.038 mW. The PEH Pepe et al. (2022 [21]) consists of a single cantilever beam but utilizes a maximum power point tracking (MPPT) scheme to enhance power output. An average power output of 2.8 mW is achieved in simulations, using vibration data as measured on the engine.

An EMEH using a non-linear mechanical spring for bandwidth widening and MPPT for power optimization is described by Paul et al. (2021 [29]). The VEH performance is evaluated on the rear part of the vehicle, in the context of a complete system powering a temperature sensor and a humidity sensor. Under harmonic excitation in a lab, the EMEH produced an average power of 552 μ W under 0.5g acceleration.

Table 1. Summary of VEH developed for use on vehicles.

Harvester type	Average Output power - lab	Lab conditions	Output power - On field/ engine	Reference
PEH - Discs	30 μ W	60 Hz @ 1 g	0.4 μ W	[19] - engine
PEH - double cantilever	0.181 mW	1 g (~2200 rpm)	0.038 mW	[20] - engine
PEH + maximum power point tracking	2.8 mW	-	average 2.8 mW	[21] - engine
PEH	18 W	60 km/h	60 km/h	[22] - suspension
PEH	332 W	-	120 km/h	[23] - suspension
PEH	0.95 mW	Low acc.	-	[24] - suspension
EMEH	340 mW	3.3 Hz, 2 mm*	-	[25] - suspension
PEH - strain	24 μ J per revolution	-	-	[26] - tire
EMEH - nonlinear magnetic springs	6 mW	60 km/h	-	[27] - tire
EMEH – plucking	13 mW	20 km/h	-	[28] - tire
EMEH - non-linear mechanical spring	552 μ W	0.5 g	-	[29] – chassis

* Displacement amplitude

1.3 Vibrational energy harvester system

A complete VEH systems consists of additional parts other than the transduction mechanism (see Figure 3 right). The standard components are rectification, filtering, regulation and storage.

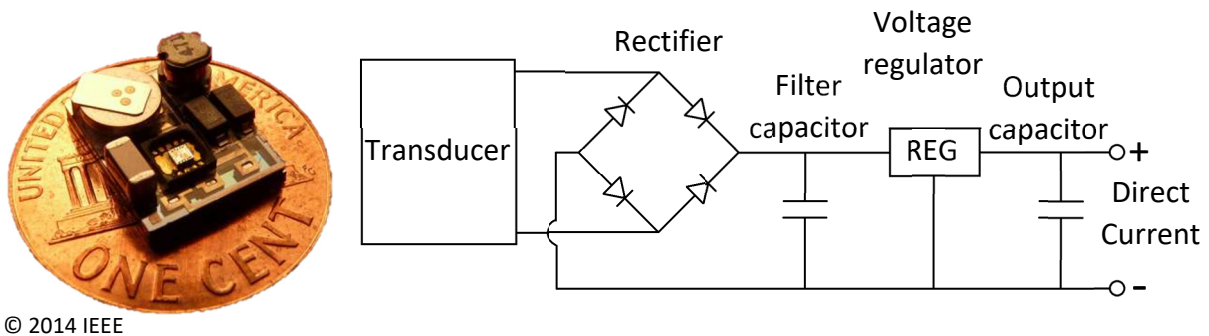


Figure 3. Left: A complete VEH system [30]. Right: Typical components required by a VEH other than transduction.

As the VEH converts mechanical oscillations the resulting current and voltage are typically of alternating polarity. As integrated circuits (IC's), such as a processor, require a direct current (DC) power supply the VEH output must be rectified, i.e., the polarity must be constant. A constant polarity does not imply constant voltage, only that it is of the same sign over time. This can be achieved by either excluding parts of the generated voltage or converting the sign. There are a number of methods to rectify a signal, either mechanically [31] or electrically by use of e.g., diodes. A common approach is a full wave rectifier bridge as seen in Figure 3, which converts the voltage to be of the same sign.

The rectified VEH output voltage is then filtered, by e.g., a capacitor to remove some of the signal variation. The voltage level is here still proportional to the amplitude of the voltage generated by the VEH transduction mechanism, which in turn depends on the ambient energy source. The unreliable voltage level together with the remaining oscillations prohibit the use of most electronics.

The filtered signal must therefore be regulated, which results in a constant DC voltage as long as the average ambient power is large enough relative the power consumption of the load. There are numerous commercial IC's which perform voltage regulation, ranging from simple a Zener diode to highly energy efficient pulse width modulation units.

Most sources of ambient energy will vary significantly in strength and can likely be under a usable threshold in recurring periods. To maintain continuous operation, the system will require a store of energy which can be used during the periods of low source energy. A capacitor at the output of the VEH regulator can fulfill this task and additionally handle any power spikes which may appear in the load circuit. Important characteristics of the charge storage unit are self-discharge rate, capacitance per gram and the number of charge/discharge cycles before failure. There are a few types of storage units which may be used, each with certain pros and cons. One promising technology is the supercapacitor, an electrochemical capacitor with high capacitance. Its most beneficial characteristics is that it allows for a very large number of charge/discharge cycles [32].

It is also likely the average ambient power is overall too low to power the desired electronics continuously. The alternatives are then to either run the application intermittently (when enough energy has been harvested) or implement a secondary battery. The VEH can then extend the lifetime of the battery by recharging when possible. The number of recharge cycles is however still limited in current state-of-the-art batteries, although advances have been made in this regard [33].

It may be necessary to include a voltage amplifier (e.g., charge pump) prior to the rectifier as many rectifiers inherently lead to a reduction in voltage. To maximize power generation, it is also necessary to regulate the load impedance [21].

1.3.1 Transduction mechanisms

There are several mechanisms which can be used to convert kinetic energy to electricity. Depending on the intended application each mechanism can be more or less suitable. Temperature sensitivity, tensile strength, complexity, and scalability are some properties which can differ between transducers and can determine which to choose for a certain application.

Mechano-electric materials exhibit useful changes in electrical properties when put under mechanical stress. Piezoelectric and electrostrictive materials are mechano-electric and give rise to charges under applied stress, which can be used to directly convert mechanical or kinetic energy to electric energy (Figure 4 left). Another example is a magnetostrictive material, that changes its magnetic permeability when under mechanical stress, which together with a magnetic field bias (Figure 4 middle), can be used to induce magnetic field variations in a coil and thus induced voltage [34,35].

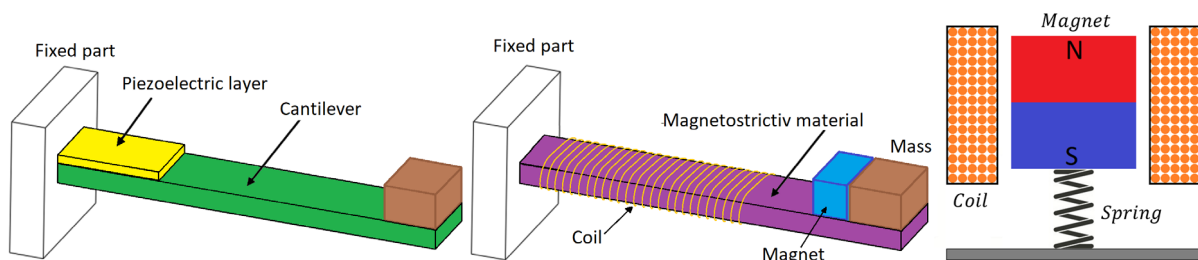


Figure 4. Left: piezoelectric cantilever with piezoelectric layer (yellow), flexible beam (green) and proof mass (brown). Middle: Magnetostrictive cantilever with coil wound magnetostrictive material, tip mass and permanent magnet. Right: Basic electromagnetic energy harvester with cylindrical magnet oscillating along coil axis [36].

Electromagnetic induction relies on Faradays law, which relates the change in magnetic flux with time in a closed loop to electromotive force (EMF), which in turn drives an electrical current. This can be achieved by, e.g., the relative displacement between coil and magnet (Figure 4 right).

Triboelectricity refers to the charge generated due to charge transfer between two different dielectric material surfaces in contact. After being brought out of contact, the induced charge difference can be used to generate a current between electrodes. The motion between

surfaces can be either vertical (Figure 5 left) or horizontal. A review of triboelectric energy harvesters is given by Wang (2013 [37]).

Electrostatic energy harvesters (Figure 5 right) make use of an initial charge within two surfaces separated by a dielectric (such as air). The initial surface charges can either be induced by an external charge source or by incorporating a charge-doped material in-between the surfaces [38]. The charge between the surfaces is initially neutral. Mechanically increasing the distance between the surfaces gives rise to a charge difference which can be extracted as electrical power.

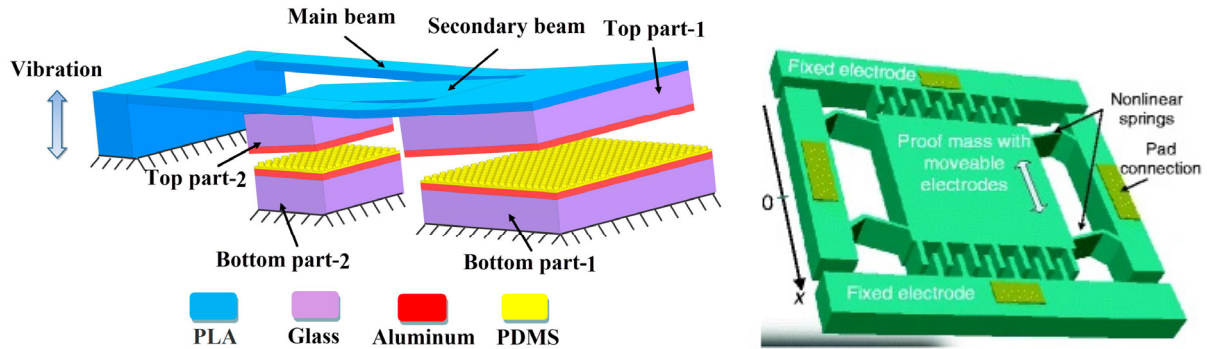


Figure 5. Left: Triboelectric cantilever with vertical motion between triboelectric layers [39]. Right: Electrostatic energy harvester [40].

In this thesis we will be focusing on piezoelectric and Electromagnetic (inductive) vibrational energy harvesting.

1.4 Optimization of power output

Most research in vibrational energy harvesting focuses on maximizing the power output. What this entails varies depending on the application.

Any VEH with an elastic component (equivalent to a spring) will generate peak power at one or two specific frequencies (resonance frequencies). Power optimization can in this regard be achieved by matching the VEH resonance frequency with the largest frequency component of the ambient vibration. Active or passive tuning schemes can also be implemented to continuously optimize the resonance frequency. The frequency spectrum of ambient vibrations will inevitably have some spread, thus achieving a wide resonance peak (i.e., large bandwidth) is also beneficial. Implementing non-linear behavior is a method which can be used to adjust the frequency range up or down as well as increase bandwidth. Examples of mechanism to induce non-linearity are bistability [41], stoppers [42], spring non-linearity [43,44] or non-linear damping [45].

There is also an optimal value of the electrical impedance of the load which is connected to the VEH. Deviation from this optimal value will either lead to a low total extracted power or most power being dissipated within the VEH. For a PEH, which can be modeled as current source in parallel with a parasitic resistance, a load impedance which is too large will lead to most generated power being dissipated within the VEH. For an EMEH, which can be modeled

as voltage source in series with a parasitic resistance, this is the case when the load impedance is too small.

Simply maximizing the power generation performance assumes there is enough ambient energy to supply this power. For cases where the ambient energy is very small it may be that most power is generated by maximizing conversion efficiency.

1.4.1 Resonance and anti-resonance

Resonance is the effect of an amplified response in an oscillating structure. Any non-rigid structure, subject to a periodic force can exhibit resonance. If there is no mechanical damping present in the structure, then exciting the structure with a frequency equal to its natural frequency will lead to resonance (conceptually illustrated in Figure 6). A simple explanation of the natural frequency is that it is the frequency at which the structure would vibrate if hit (or plucked in the case of a guitar string). In reality it is a bit more complicated as the structure will have a number of “harmonics” at which the excitation frequency also leads to resonance. There is also the possibility of the structure having multiple degrees of freedom. A beam may for example both bend and twist. If, in this case, the bending and twisting are dependent of each other we have a system of two coupled oscillators. There can be any number of coupled oscillators in a vibrating structure and for each coupled oscillator, the structure will exhibit an additional resonance peak. We could complicate this further by again considering the higher order harmonics for each oscillator.

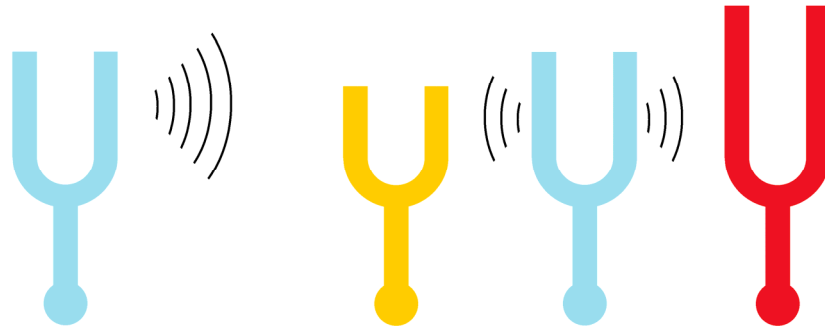


Figure 6. Basic principle of resonance between tuning forks of equal geometry.

When analytically modelling a VEH it is often simplified as a single degree of freedom (SDOF) mechanical oscillator coupled to an electrical domain. The electrical domain is typically also idealized and contains only one reactive component (a capacitance in the case of a PEH and inductance in the case of an EMEH). As an electrical oscillator requires both an inductance and capacitance, the idealized VEH in the electrical domain is not an oscillator. Based on this modelling a VEH will only have one resonance frequency (with high order harmonics still possible).

As described in paper II of this thesis, a SDOF VEH can be designed to have two power peaks as a function of excitation frequency. The second peak is a result of the systems anti-resonant frequency. While the resonant frequency corresponds to the systems state of minimum impedance (i.e., an oscillation amplitude maximum), the anti-resonant state corresponds the state of maximum impedance (oscillation amplitude minimum). The anti-resonant state

occurs when the VEH exhibits a maximum in damping, which occurs when the transfer of energy, from the mechanical domain to the electrical domain, is at a maximum. This is equivalent to a maximum in electrical damping. An example of measured resonance and anti-resonance in a PEH is given by Colin et al. (2013 [46]). A further explanation of resonance and antiresonance, and their relations, can be found in the IEEE Standard on Piezoelectricity [47] or in the textbook by Priya and Inman [48]. Although the explanations are centered around PEH they hold for any VEH (given that some expressions need to be modified).

1.4.2 Stochastic resonance

The forms of resonance described in the previous section are based on harmonic base excitation. In reality the base excitation of a VEH will often be noisy to a large degree, but with possible harmonic components. This type of vibrational environment can be ideal for a VEH implementing stochastic resonance.

Stochastic resonance can only be utilized in a bistable or multistable VEH, i.e., a VEH with at least two states of minimum potential energy. The benefit of such a system in a noisy environment is that a sufficient noise level can induce oscillations between the two potential minima, when the harmonic component is too small. The theory of stochastic resonance is explained in detail by Rajasekar et al. (2016 [49]). A practical example using a snap-through buckling beam for bi-stability is given by Ando et al. (2020 [50]). Chapter 2.2 gives an in-depth example of a bi-stable rotational VEH utilizing stochastic resonance.

1.4.3 Impedance matching

From electrical circuit theory it can be derived that there is an optimal resistance of the load, at which most power is dissipated by the load. For a non-optimal load, a significant portion of the energy generated by the VEH will be dissipated as heat by the intrinsic impedance of the VEH. The expression for intrinsic impedance differs between different types of VEH. For an EMEH the impedance is a result of an inductance in series with the coil wire resistance. For a PEH it is a capacitance in parallel with a resistance resulting from two parallel plates (the electrodes) and a dielectric (the piezoelectric material) in between.

Only taking into account circuit theory, the optimal load resistance would equal the VEH equivalent circuit impedance. It can however be derived that for a VEH one must also include a term proportional to the electrical damping of the system. For the simplified case of a purely resistive load, there is no phase difference to consider, between load and VEH. This thesis does not consider the case of a reactive load.

Both impedance and electrical damping are frequency dependent. For a practical case, where the excitation frequency is likely noisy and shifting it is typically beneficial to have a dynamic and adaptive load. MPPT is based on this idea and is well established in literature [51] and can be found as a feature in commercial power management units.

1.5 Scope

The scope of this thesis is to explore the use of piezoelectric and electromagnetic vibrational energy harvesters as power source for sensors in vehicles. The thesis will also describe the basic principles and characteristics of these systems. The thesis will not evaluate the complete VEH system in detail and will thus not delve into the research regarding rectification, impedance matching, power management or energy storage.

Chapter 1 of this thesis introduces vibrational energy harvesting in general and its applications in the automotive industry. An overview of a complete VEH system is given and the key characteristics are explained.

Chapter 2 describes the fundamental principles of the piezoelectric effect and gives a review of its implementation for sensors in vehicles. The design, implementation, and results for a PEH utilizing stochastic resonance to power a strain sensor on an engine flex plate, is also described.

Chapter 3 describes the fundamental principles of magnetic induction and gives a review of its implementation. The design, implementation, and results for an EMEH powering a sensor on a belt buckle is here described.

Chapter 4 presents analytical modeling methods based on lumped and distributed models and gives an in-depth analysis of the results of such modelling for piezoelectric and electromagnetic energy harvesters.

Chapter 5 gives a discussion, conclusion and description of future work to be done, based on the results and experiences gained from the current thesis work.

2.1 Introduction to piezoelectricity

Piezoelectricity, the phenomenon where certain dielectrics become polarized under tension or compression and vice versa, was first demonstrated by the brothers Jacques and Pierre Curie in 1880 [52]. Their discovery was a result of their research into pyroelectricity, where they examined the polarization effect in semi-symmetrical crystals due to heat. They found that a polarization could also be achieved by applying pressure along certain axis of the crystal. The first practical serious application of this physical phenomenon was in Sonar devices during the first world war [53]. The Sonar was invented to detect submarines, utilizing a piezoelectric element to both generate and measure acoustic under water waves. Since then, piezoelectric elements have found many uses as sensors, actuators and energy harvesters. Perhaps one of the most important uses is as a clock generator for processors, without which they would not function.

To possess the property of piezoelectricity the material must have a non-centrosymmetric arrangement of its atomic or molecular structure [54]. Centro-symmetry refers to structures which are identical on opposite sides of an axis, for any given point. Figure 7 shows a simple model for an intuitive explanation the piezoelectric effect in crystals, proposed by Meissner A. in 1927 [55]. The model is based on quartz, which has a unit cell structure that is non-centrosymmetric. Under stress-free conditions the unit cell is neutral but becomes polarized when subject to tension or compression. The natural crystal structure in quartz is such that the polarization of unit cells is aligned through the material, thus leading to a net polarization in the bulk of the material.

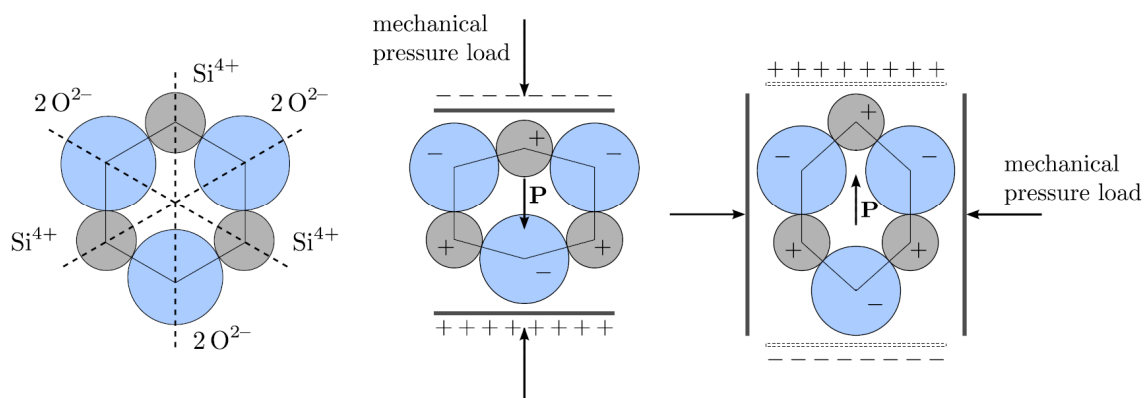


Figure 7. Crystal unit cell model for Quartz and the effect of applying pressure [56].

Piezoelectricity can also be induced in some ceramics. These ceramics have crystal unit cells which become non-centrosymmetric and form dipoles under a certain temperature [57]. Examples are perovskite, lead titanate (PTO) and lead zirconate titanate (PZT), all of which have the same structure (see Figure 8). Within the ceramic material there will be regions where the electric dipoles are approximately aligned. Such a region is called a Weiss domain. The orientation of Weiss domains in an untreated ceramic is random. By applying a strong electric field over the ceramic, while keeping it heated to facilitate domain movement, all the Weiss domains can be aligned. After cooling the alignment is to a high degree maintained. The ceramic will now behave as modeled in Figure 7. Compared to Quartz however, these piezoelectric ceramics can achieve a much stronger piezoelectric effect.

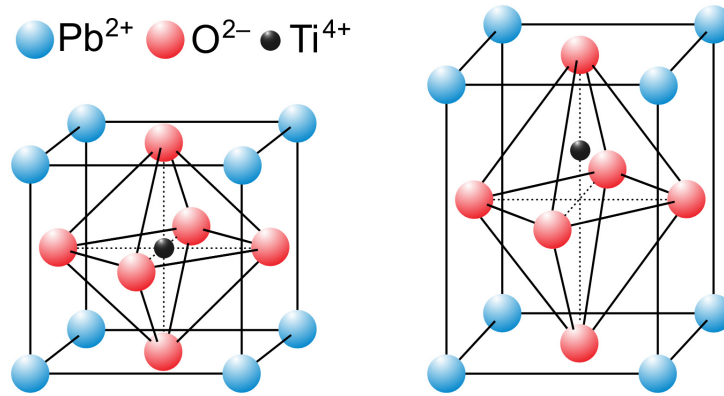


Figure 8. Left: PTO above the Curie temperature with centrosymmetric unit cell. Right: PTO below Curie temperature with non-centrosymmetric unit cell [57]. Image source [58].

Piezoelectricity is not restricted to occurring in crystalline materials [54,59]. The phenomenon has been observed naturally in some polymers such as DNA and various proteins and can also be induced in synthesized polymers.

The piezoelectric effect goes both ways; applying stress the material generates an electric displacement (i.e., charge) and applying an electrical field generates strain with the material (compression or tension). Stress to charge is called the direct piezoelectric effect. Electric field to strain is called the inverse/converse piezoelectric effect.

An important characteristic of the piezoelectric effect is that it is linear [53] (unlike the similar electrostatic effect which is cubic). A constant defining this linear proportionality is the piezoelectric constant, d , coupling the electric charge density displacement D to stress T and strain S to electric field E . Considering the 3 dimensions of space and rotation in each dimension, d becomes a 3rd rank tensor, D and E are 3x1 vectors and T and S are 3x3 matrices. d is transposed for the inverse piezoelectric effect. These linear relationships are given by Equation (1) and Equation (2).

$$D_i = d_{ijk} T_{jk} \quad (1)$$

$$S_{ij} = d_{kij} E_k \quad (2)$$

To derive the actual charge displacement or strain we must include the effects from the elastic and electric nature of the material. For the inverse effect we include a term according to

Hooke's law (Equation (4)) and the natural relationship between charge density displacement and electric field within any dielectric (Equation (3)). Here ε is the dielectric permittivity, a 3x3 matrix, and s is the elastic compliance, a 4th rank tensor.

$$D_i = \varepsilon_{ij}E_j \quad (3)$$

$$S_{ij} = s_{ijkl}T_{kl} \quad (4)$$

The constitutive strain-charge equations (Equations (5) and (6)) describing the piezoelectric material is given by the combinations of Equation (1) and (2) and Equation (3) and (4). The tensor ranks can be reduced by using Voight notation in which the rotational elements are combined, e.g., $T_{11} \rightarrow T_1$, $T_{22} \rightarrow T_2$, T_{23} and $T_{32} \rightarrow T_4$, T_{13} and $T_{31} \rightarrow T_5$ and T_{12} and $T_{21} \rightarrow T_6$. T and S can now be expressed by 1x6 vectors, d as a 3x6 matrix and s as a 6x6 matrix. To clarify, using Voight notation, indices 1 to 3 correspond to the 3 dimensions of space, while indices 4-6 correspond to rotation.

$$D_i = d_{ij}T_j + \varepsilon_{ik}E_k \quad (5)$$

$$S_j = s_{jl}T_l + d_{ji}E_i \quad (6)$$

It is important to note that the values of ε_{ik} and s_{jl} are those derived under the absence of piezoelectric effects. ε is derived under zero or constant stress, equivalent to unclamped or mechanically free conditions and s is derived under zero or constant electric field, equivalent to open circuit conditions [60].

2.2 Piezoelectric energy harvester research

In the early days of piezoelectric research, the viable applications were limited due to the few available piezoelectric materials with notable electromechanical coupling (typically Quartz or Rochelle salt). With the discovery of barium nitrate and later PZT a significant improvement in coupling factor was achieved. These were ceramic materials with which the composition could be tailored to suit the need of the application.

The "thin film cantilever beam" is today the most commonly applied type of piezoelectric energy harvester. It consists of a substrate (e.g., silicon) with a thin film of piezoelectric material deposited on top (e.g., PZT). Some reasons for the cantilevers popularity in this sense could be the relative simplicity in design and the possibility to accurately predict the system characteristics with a combination of Euler-Bernoulli beam theory (see chapter 4) and the constitutive strain-charge equations.

The basic cantilever configuration has some drawbacks. The resonance frequency typically increases with decreasing size, as the beam length gets shorter. Compensating by reducing thickness leads to a reduction of the generated charge. The bandwidth is also relatively small in comparison to the width of an in-situ vibration spectrum. Thus, research focuses to overcome these drawbacks by various methods. The following paragraphs will give examples of macro-sized VEH implementing different methods to optimize the frequency response.

Although the average power output will be specified in each example, it should not be used as a performance metric as neither size nor excitation magnitude is considered.

A fairly straight forward approach to increasing the bandwidth is implemented by Kim et al. (2020 [61]). The electrodes of four single layer thin film PZT cantilever beams, each with a shift in natural frequency, are connected in parallel in the electrical domain. The frequency response of each is essentially superimposed, leading to a large increase in the frequencies where a useful power output can be achieved. Using an array configuration where all the PZT layers are facing the same direction (e.g., “up”) leads to four separate bands of viable power. By alternating PZT layers with face “up” and face “down”, the power in-between the resonance peaks can be increased to viable levels, at the cost of peak power. As an example, one of the array configurations achieved two full width at half maximum (FWHM) bands of 8 Hz and roughly 3 mW at 1.5 g excitation (in the range 110 Hz-130 Hz). A related approach is to use multiple beams coupled in the mechanical domain as well as the electrical domain, as described by Bouhedma et al. (2020 [62]). This system also implements magnetic coupling for active frequency tuning. A power output of 0.5 mW at 0.5 g is achieved with a FWHM of at most 4 Hz.

The review of magnetically coupled PEH, by Jiang et al. (2021 [63]) gives several examples of different magnetic coupling schemes leading to monostable, bistable and multi-stable systems. Each of these can be used to tune the frequency response. The bistable and multi-stable configurations have the benefit of larger mass-displacement due to inter-well oscillations. Sun et al. (2022 [64]) describe a PEH which achieves quad stability by the force interaction between a ring magnet and square magnet. The prototype of this PEH shows a measured power output of 19 μ W at 1.5 g.

Non-linear characteristics in a VEH can also be achieved by mechanical springs with non-linear stiffness, typically achieved by a certain geometry of the spring. The PEH by Pertin et al. (2022 [44]) implements a tapered mechanical spring. An output power of 2.6 mW at 0.9 g is achieved, with a specified bandwidth of 9 Hz. An orthonormal planar spring is used in the PEH by Dhote et al. (2019 [65]), which achieves a bandwidth of 35 Hz with a peak-to-peak voltage of 4V at 0.8g excitation amplitude. The power output was in this case not clearly specified. Chen et al. (2022 [66]) describe a PEH with a relatively large bandwidth of 13 Hz, considering the center frequency of approximately 40Hz. This PEH uses perforated segments of a clamped-clamped beam to achieve non-linear stiffness. An average output power of 0.184 mW is achieved.

Table 2. Summary of reviewed piezoelectric energy harvesters.

Harvester type	Output power / voltage / Bandwidth	Conditions Acc. @ resonance freq.	Reference
Multi-beam	3 mW / 8 Hz	1.5 g @ 115 Hz and 126 Hz	[61]
Multi-beam	0.5 mW / 4 Hz	0.5 g @ 63 Hz and 76 Hz	[62]
Quad stable	19 μ W	1.5 g *	[64]
Tapered mechanical spring	2.6 mW / 9 Hz	0.9 g @ 150 Hz	[44]
Orthonormal planar spring	4 V peak-to-peak / 35 Hz	0.8 g *	[65]
Perforated segments of clamped-clamped beam	average ca. 0.2 mW / 13 Hz	0.3 g @ 40 Hz center frequency	[66]

* Resonance frequency not applicable

2.3 Piezoelectric energy harvester for engine sensor

In any vehicle there are several rotating components. Rotations with an axis perpendicular to earth's gravitational field allow for a simple mechanism to induce an oscillating force. For a small VEH with small proof mass the force amplitude is however quite small. The vibrations from road roughness and engine dynamics together with the small periodic gravitational force are a good combination for implementing a stochastic resonance VEH. The work described here [67] explores the possibility of using a simple cantilever beam on the engine flexplate to power a strain sensor (see Figure 9).

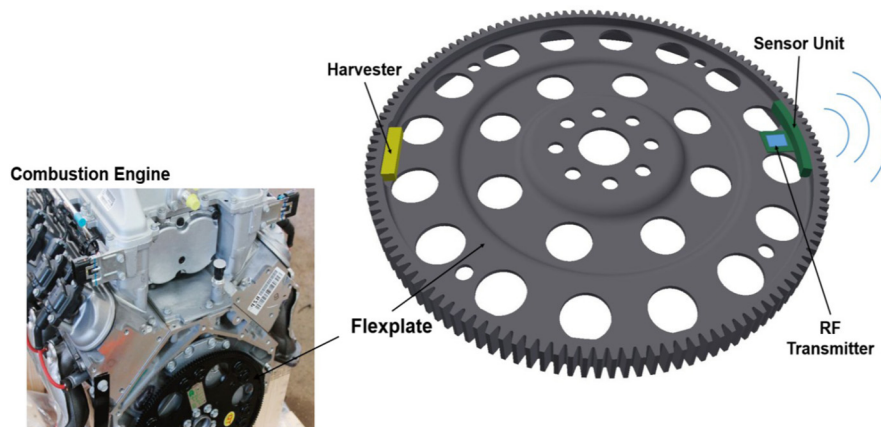


Figure 9. Placement of stochastic resonance VEH and strain sensor on flexplate within engine.

In rotating systems there are multiple sources of excitation that can be harvested, such as alternating gravity direction, centrifugal force and the rotational movement itself, all well defined by the rotation speed. There are various designs of rotational VEH in the literature; utilization of separate parts by using magnetostatic coupling between the static and rotating parts [68]; or the VEH is mounted entirely on the rotating part of a system, using a magnetostrictive or piezoelectric transducer and the alternating gravity of the rotation as a source of excitation [69]; or a passively tuned PEH using the centrifugal force to tune the resonance frequency [70] obtaining a tenfold increase in bandwidth when compared to a cantilever with constant axial force.

Another source of energy in these rotating systems is vibration that is exploited in a periodically modulated bistable system. This approach allows for higher energy output than monostable systems under the same excitation, e.g., by using a piezoelectric cantilever with a magnet tip mass combined with another magnet [71]; or increases bandwidth significantly compared to non-self-tuning concepts, when using the centrifugal force to achieve bistability [72,73].

The rotational PEH described in this chapter is a lightweight harvester mounted entirely on the rotating part, with dimensions of 40 x 8 x 6 mm. The concept is based on a piezoelectric beam with a proof mass that is inwards oriented to create a bistable system using centrifugal force as schematically shown in Figure 10. This design allows the harvester to be much smaller than previous designs [71,73] as it does not need any magnets to create the bistable system nor the coils for power generation.

The simulations of the rotational PEH were performed in both COMSOL and MATLAB using the values of a commercial 2-layer PEH with resonance at 98 Hz. The mentioned PEH was used in the experiments.

From the equation of motion simulated in MATLAB it can be seen that this system has a bistable behaviour (Figure 11 left and right) where the velocity of the cantilever's end point is plotted against its displacement for the cases without and with white noise signal as vibration, respectively.

The simulations for power as a function of rotation frequency are presented in Figure 12, where the values are averages of multiple runs as the occurrence of resonance is dependent on white noise and thus is random. The peak output is 370 μW and the bandwidth is 2.44 Hz (equivalent to a bandwidth of 146.4 rpm).

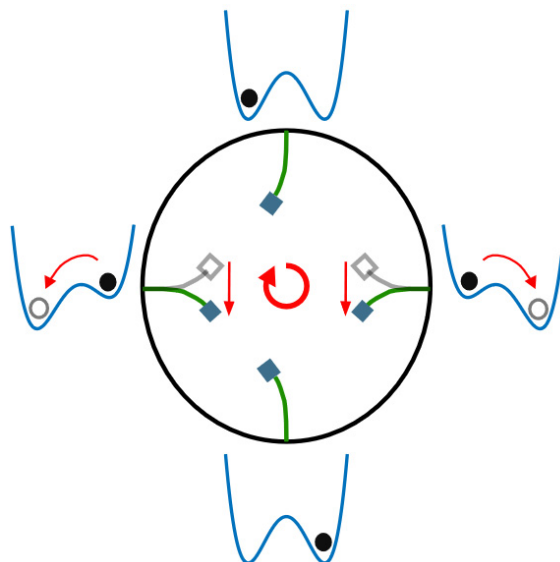


Figure 10. Schematic of piezoelectric cantilever positioning on the rotating part and visualization of the change in potentials during one rotation of a centrifugal force induced bistable system [67].

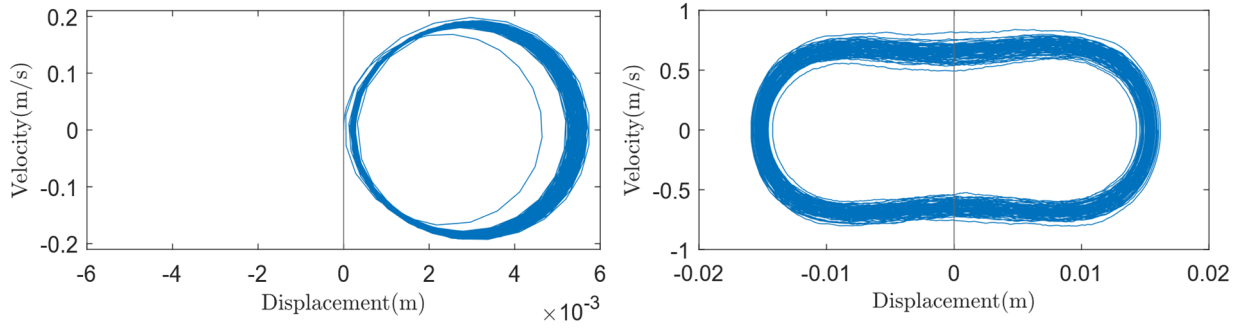


Figure 11. Left: Inter-well movement only due to vibrations; Right: Movement between stable positions under periodic forcing and vibrations [67]

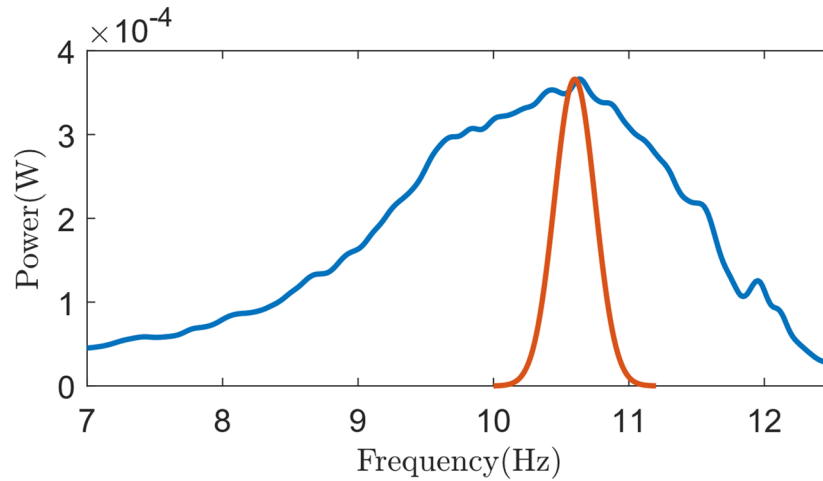


Figure 12. Increase in bandwidth (blue line) of the bistable EH as compared with a standard harvester (red line) having the same Q-factor as obtained from the measured damping ratio (normalized to match the power obtained in the simulations) [67].

To validate simulation results, lab measurements were carried out on a simple prototype. A miniature electrodynamic shaker (Modal Shop 2007E), driven by a SmartAmp power amplifier (Agilent 2100E21-100) was used to generate a sinusoidal excitation for the harvester. The response of the harvester was recorded using both an oscilloscope (PicoTechnology 2000 series) to measure the output voltage and a laser distance sensor (Panasonic HL-G1) to measure the displacement of the harvester (Figure 13 left).

Measurements were performed to compare the real bending of the cantilever beam to the theoretical calculations used in the simulations when a static force equivalent to the centrifugal force is applied to the harvester. Two measurements setups were implemented. The first was a simple setup, with the cantilever beam being pushed against an EKS Electronic Scale. The tip displacement and force could in this way be accurately measured (using the laser distance sensor) under static conditions. However, as the tip is in this case not strictly free, the results can contain significant error. For the second setup the harvester was placed in a rotating system with the proof mass facing inwards as seen in Figure 13 right. A DC motor (Micro Motors, RH158 12V) was used to drive the rotation and the movement was recorded by a digital camera (Nikon D5300). In this case the beam tip is free. Although this setup replicates the centrifugal force of the real application, it was error prone in regard the measuring the tip displacement.

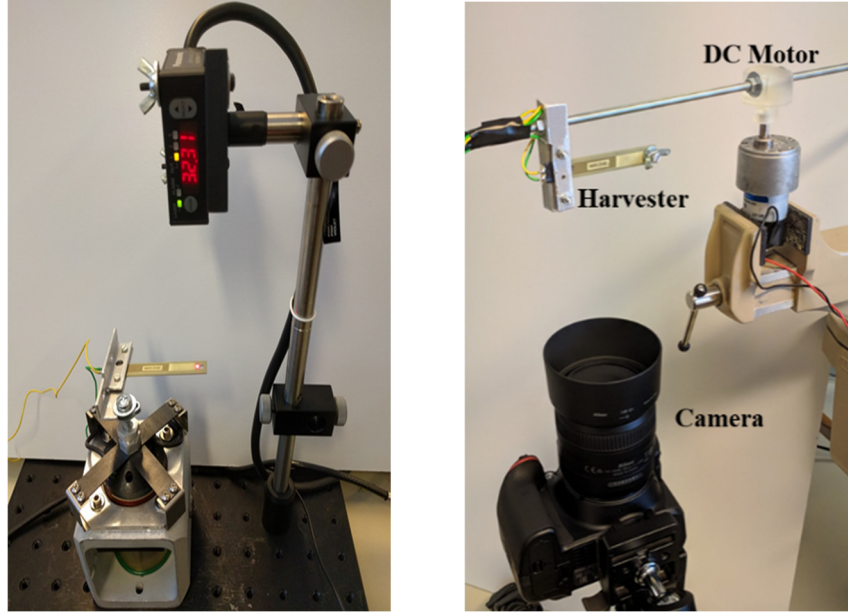


Figure 13. Left: Experimental setup for EH characterization. Right: horizontal rotation testing (The camera is pointing up) [67].

The resistance sweeps that were performed at resonance both in COMSOL and experimentally are shown in Figure 14, with the peak power at approximately 70 k Ω in both cases. The good agreement between these datasets indicates that the electrical characteristics of the COMSOL model are close to those of the experimental setup.

The theoretical values for the equilibrium positions as a function of rotation frequency are shown in Figure 15 with continuous lines. The experimental data shown in Figure 15 represents an empirical upper limit buckling frequency (red circle), the calculated lower limit of the buckling frequency (green circle), and the displacement at specific rotation speeds (blue circles). The experimentally determined buckling frequency, using the scale setup, will likely result in an over estimation as the movement of beam tip is to some degree hindered by friction against the scale. The experimental displacement of the beam has increasing error margins with the rotation speed due to a too simple measurement setup. With this in consideration, the bistability simulations show good agreement with experiment.

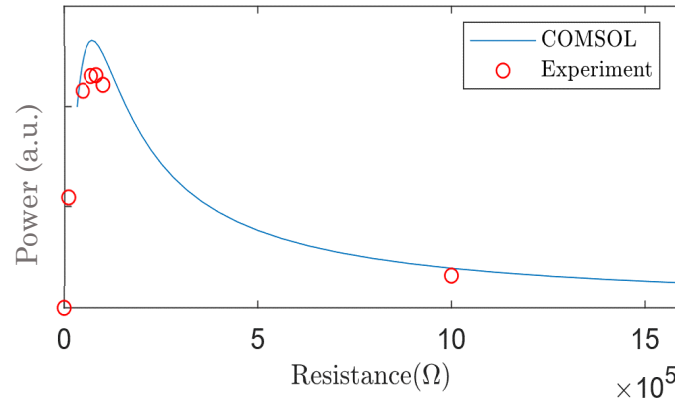


Figure 14. The resistance sweeps in COMSOL and experimental results showing the power at resonance dependent on resistance of a harvester without proof mass [67].

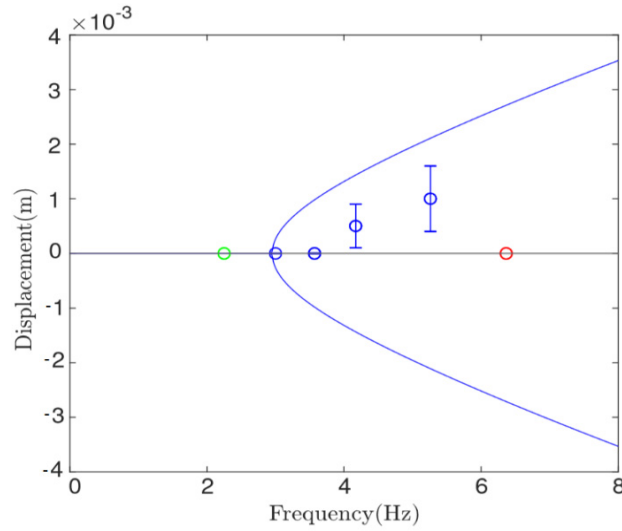


Figure 15. Theoretical (line) and experimental bending results for the displacement of piezo proof mass vs frequency. Red circle is the measured equivalent buckling frequency using the scale setup. Green circle is the calculated lower limit buckling frequency. Blue dots are the measured displacement in the rotating setup [67].

With the presence of a double potential as generated by the buckling of the harvester the difference in movement when comparing movement inside one potential well and movement between the potentials wells is significant. When comparing the results in Figure 11 left and right, the top velocity is not only increased but also kept during a longer time as the distance is significantly increased as well. As the instantaneous power is dependent on the velocity squared there is no doubt that the occurrence of a bistable system, under periodic modulation, can increase the mechanical power available in a system.

The work described here provides a proof-of-concept for a miniaturized rotational energy harvester mounted on a flexplate. The results show that the vibrationally excited bistable EH, under periodic modulation, significantly increases power output compared to a monostable system. Likewise, an increase in bandwidth is gained from the passive tuning by centrifugal force. The EH described in this work is significantly reduced in size compared to similar state-of-the-art technologies, by utilizing an inwards oriented beam under alternating gravity to achieve bistability and a piezoelectric element for energy harvesting.

3.1 Introduction to electromagnetic induction

All electromagnetic energy harvesters use the principle of Faradays law to convert kinetic energy to electrical power. That a magnetic field can generate current was hinted at by the experiments of François Arago in 1824. His experiment, showing “Arago rotation” showed a magnetized needle which rotated when a copper disc was rotated in close proximity (with the disk in parallel with the needle). The properties of electromagnetics were not well understood at the time and thus the reason for the Arago rotation was under much debate [2]. The experiments performed by Faraday in 1831 essentially provided all the laws governing electromagnetic induction [1] shedding new light on old problems. Faradays describes his experiments in “V. Experimental researches in electricity” [74], in which he writes:

“Upon obtaining electricity from magnets by the means already described ..., I hoped to make the experiment of M. Arago a new source of electricity; and did not despair, by reference to terrestrial magneto-electric induction, of being able to construct a new electrical machine”

The mathematician Clerk Maxwell derived a mathematical formulation [75] for electromagnetic induction based on Coulombs law for electrostatics and results from experiments by Faraday, as well as Lenz. This expression is known as Faradays Law and is given by Equation (7), which states that the line integral, along a closed loop, of the electric field is equal to the time derivative of the flux in area bounded by the line. Here ϕ is the magnetic flux, E is the electric field and B is the magnetic flux density. Equation (7) is also called the induced electromotive force (EMF, with the units of Volts). Equation (8) is an alternative form of Faradays law [75].

$$\oint \vec{E} \cdot d\vec{s} = \frac{d\phi}{dt} \quad (7)$$

$$\nabla \times E = \frac{dB}{dt} \quad (8)$$

To determine the current generated from moving a magnet close to a coil, the magnetic field from the magnet, in the region of the coil, must first be determined. The magnetic field from a cylindrical magnet is equivalent to the field produced by a tightly wound ideal solenoid. The field can be determined using Biot-Savarts law [76], which is an expression for the magnet

field as a result of a constant current. An alternative is to treat the magnet as a volume of infinitesimal magnetic dipoles, from which the effect of each is integrated over the volume [77]. Equation (9) gives the expression for the magnetic field density along the symmetry axis of a cylindrical magnetic. B_r is the magnetic remanence of the magnet, L_m and D_m are the length and diameter of the magnet and x is the distance from the centre of the magnet.

$$B(x) = \frac{B_r}{2} \left(\frac{x + L_m/2}{\sqrt{(x + L_m/2)^2 + (D_m/2)^2}} - \frac{x - L_m/2}{\sqrt{(x - L_m/2)^2 + (D_m/2)^2}} \right) \quad (9)$$

Equation (9) together with Equation (7) or (8) can be used to approximate the voltage induced in coil from a magnet moving along the axis of the coil. This requires the simplification that the z-component of the magnetic field has an insignificant variation within the radius of the coil. By integrating the time differential of magnetic field density, over the length of the coil, and multiplying with area, A , and winding density, n , the generated voltage is given by Equation (10).

$$V_{IND} = nA \int \frac{dB_z}{dt} dx \quad (10)$$

Similarly to electrical current, the magnetic flux will take the path of least resistance. In electromagnetic theory the term reluctance is used instead and is a function of the magnetic permeability, length and area of a volume. Materials with high permeability can be used to guide magnetic flux, constituting a magnetic circuit. The driving “force” in the magnetic circuit is called the magnetomotive force [78] and can be seen as an analogy to EMF. Magnetic circuits are for example implemented in various motors, actuators [79] and transformers.

3.2 Research in electromagnetic energy harvesting

As mentioned in the introduction of this thesis, the principles of energy harvesting by magnetic induction date back to the late 1800s. During the initial decades of development of electrical generators, size was not a large issue, nor was the frequency response as the input was typically clearly defined. The research field of vibrational energy harvesting put the electrical generator in a new context with new challenges. Researchers in the field of vibrational electromagnetic energy harvesters face the same challenges as those in the field of vibrational energy harvesting in general, such as achieving a large bandwidth, high power output, low resonance frequency and small size. It is also often stated that the typical EMEH is relatively bulky but benefits from a large electromechanical coupling factor.

An important factor determining the potential power output of an EMEH is the magnetic field gradient. Some research is therefore focused on maximizing this aspect. Li et al. (2021 [80]) achieve a large gradient by a planar array of $M \times M$ magnets, with a 180° polarity shift between each row of magnets. The magnet array oscillating above a planar array of coils produces an average output power of 284 mW at 1 g and approximately 20 Hz. Amjadian et al. (2022 [81]) use a single coil sandwiched between two $M \times M$ planar magnets arrays. The

polarization shift schemes explored by Amjadian et al. are more complex than those used by Li et al., yet the best performing array uses the same polarization scheme as Li et al. 500 mW is achieved at 0.1 g and approximately 61 Hz. Ordoñez et al. (2022 [82]) utilizes a stack of 3 magnetic rings, with 90° polarity shifts between each. This configuration increases the gradients of magnetic flux density within the ring-stack. Power is generated from a coil on a spring within the ring-stack. Their VEH generates 3.61 mW at 0.03 g and 61.7 Hz.

Non-linear spring action is implemented in some EMEH to increase bandwidth and/or reduce the resonance frequency. A VEH using a magnetic spring system, which is inherently non-linear, is described by Nguyen et al. (2013 [43]). An oscillating magnet is “trapped”, by opposite polarities, between two stationary magnets. Two differentially coupled coils, summing the generated voltage of each, are placed around the path of the oscillating magnet. A model, verified by measurements, shows a potential power output of 170 mW at 1.25 g and 16 Hz. A review on this type of VEH is given by Carneiro et al. (2020 [83]). A nonlinear magnetic torque spring is used in a wrist worn VEH described by Cai et al. (2021 [84]). Power generation of 151 μ W was achieved during simulations of walking with a step frequency of 1.3 Hz.

Xu et al. (2022 [85]) achieve a bi-stable EMEH by replacing the stationary cylindric magnets, typically used in a magnetic spring system, with axially polarized ring magnets. The bandwidth of this EMEH increases with decreasing distance between the ring magnets, at a cost to peak power. The EMEH generates a peak power of 6.02 mW at 9.5 Hz and 0.5 g. Another approach to bandwidth broadening is to use multiple oscillating elements, with different resonance frequencies. A double cantilever type EMEH is described by Foong et al. (2022 [86]).

Table 3. Summary of reviewed electromagnetic energy harvesters.

Harvester design	Output power	Conditions Acc. @ resonance freq.	Reference
Magnet and coil array	284 mW	1 g @ 20 Hz	[80]
Magnet and coil array	500 mW	0.1 g @ 61 Hz	[81]
Stacked magnet rings	3.61 mW	0.03 g @ 61.7 Hz	[82]
Magnetic spring system	170 mW	1.25 g @ 16 Hz	[43]
Magnetic torque spring	151 μ W	1.3 Hz (Pseudo walk) *	[84]
Bi-stable	6 mW (peak power)	0.5 g @ 9.5 Hz	[85]
Multi-beam	119.6 mW	0.1 g @ 25 Hz	[86]

* Measured with mechanical system to emulate walking. Step frequency of 1.3 Hz.

3.3 Electromagnetic energy harvester for safety sensor in belt buckle

An electromagnetic energy harvester for a safety sensor was developed in this thesis. The main goal was to reduce as much as possible or even to totally remove the electrical cables used for powering a sensor in the safety belt (Figure 16) and for transmitting the sensor’s data. This was to be achieved by harvesting the ambient vibrations in the belt-buckle.

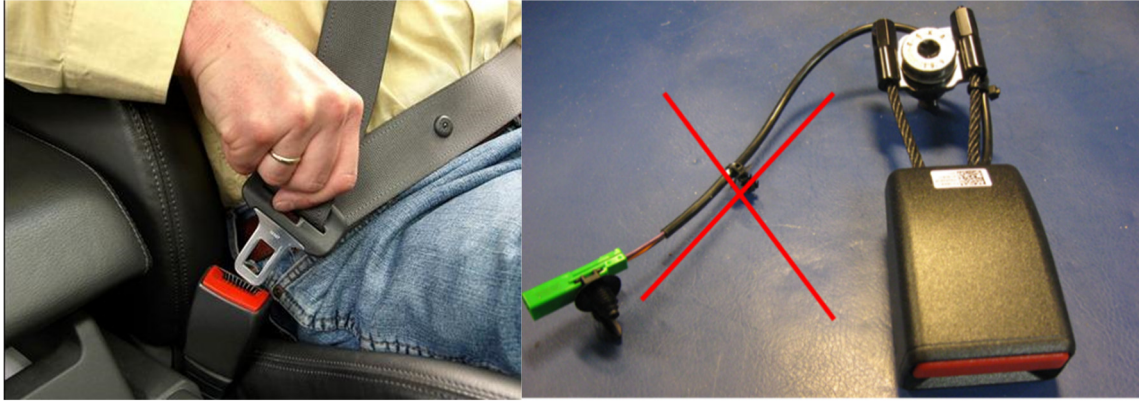


Figure 16. Belt buckle including cable harness and connector.

The safety belt should give information regarding the ‘user status’ and the ‘standby status’. Thus, the energy harvesting system, acting as a power supply, should fulfil its operating requirements for these test cases:

- Airport parking – 4 weeks
- Several buckling / unbuckling with short driving (e.g., taxi)
- Not so many buckle / unbuckle (e.g., highway driving / baby chair)
- How fast after buckle/unbuckle will the system work
- Frequency of measurements – Buckle/Unbuckle

In this thesis the work is aimed towards maximizing the harvested energy, and thus frequency of measurements, during extended periods between buckling sequences, e.g., driving on the highway. Figure 17 and Figure 18 show two examples of accelerometer measurements performed on a belt buckle. The speed and road conditions vary between the data-sets, which is clearly reflected in the corresponding frequency plots. A VEH for these conditions will need to be able to harvest vibrations well below 100 Hz and preferably have a tunable optimal frequency down to just a few hertz as well as a significant bandwidth.

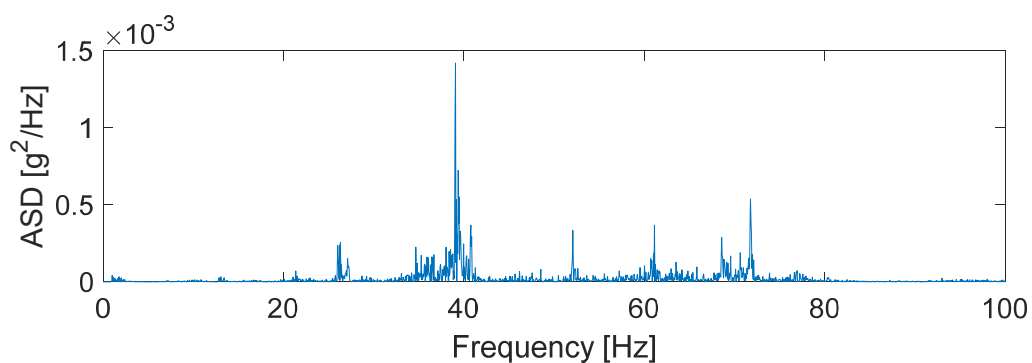


Figure 17. Acceleration spectral density of measured acceleration in a Volvo V60, driving on a highway at 70 km/h.

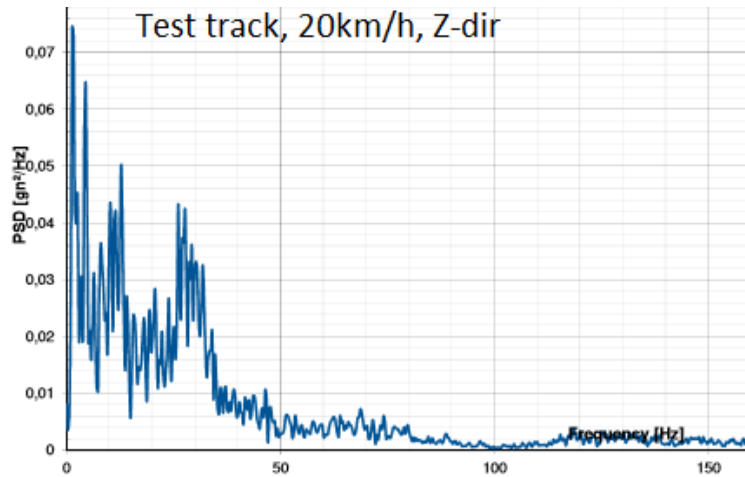


Figure 18. Power spectral density of measured acceleration in a compact Multi-Purpose Vehicle, driving on a test track at 20 km/h.

The average acceleration for the data-set corresponding to Figure 17 is only 0.38 m/s^2 , which for a linear system with small mass leads to very small displacements within the VEH, unless the stiffness of the VEH is very small. One solution to this problem is to introduce a non-linearity into the system. A novel yet simple method to achieve this was to make use of the nonlinear relationship between force and magnetic flux in the air gap of a magnetic circuit. The gap force is proportional to the square of the magnetic flux through the gap. Figure 19 shows the chosen design to implement this concept.

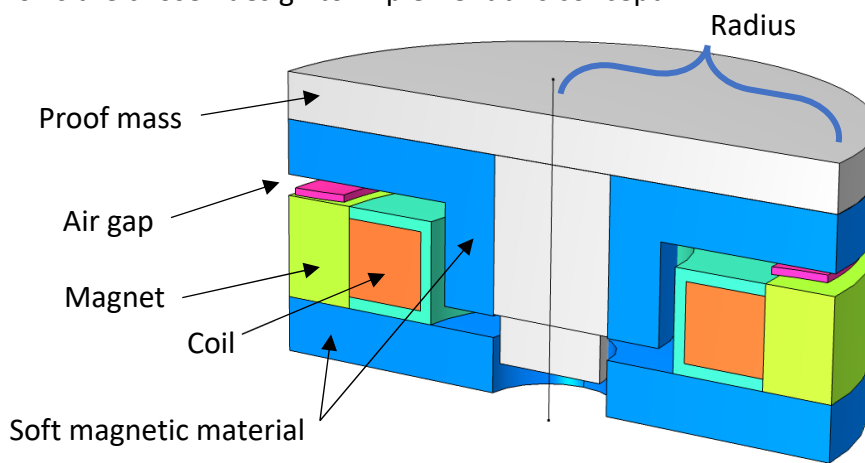


Figure 19. Electromagnetic energy harvester concept design with ideal spring placement. Schematic of geometry and constituents.

The EMEH described in paper I can be thought of as a magnetic circuit with a permanent magnet to generate magnetomotive force, a core to guide the flux and a variable air gap to control the reluctance of the magnetic circuit. The flux in the magnetic circuit is passed through a coil. Varying the reluctance of the circuit leads to a varying flux through the coil and thus current is generated. The variable air gap is achieved by dividing the magnetic circuit in two parts, kept apart by a mechanical spring while the magnetic flux works to close the gap. As the spring-force is linear and the attractive magnetic force is non-linear, with respect to gap length, the relationship between an externally applied force and gap length displacement becomes nonlinear.

The initial idea was based in the principles outlined in Figure 20, showing the quadratic and linear force vs distance relationship for the magnetic force and spring force respectively. At this point hysteresis effects in the magnetic core had been neglected.

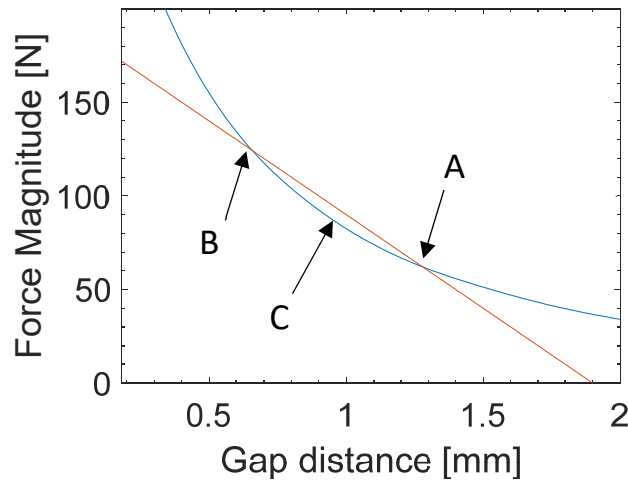


Figure 20. Magnitude of opposing forces. Blue: Magnet force. Red: Spring force. A: Stable equilibrium. B: Unstable equilibrium. C: Local maxima in restoring force.

The method to validate and develop this concept was to build both a physical prototype (see Figure 21) and an equivalent FEM model in which complex effects could be considered, such as hysteresis and eddy currents in the core. Measurement result from the prototype would confirm the validity of the FEM model, which could then be used as an optimization platform and to simulate other types of excitations. The first step in characterizing the prototype system was to measure the force at varying air gap. A custom test-rig was built to hold the relevant components (see Figure 22 right). Magnet and one core component were mounted statically. The second core component was mounted on a rod passing through the center of the magnet and resting on a vertically adjustable base. The force was measured between rod and base. Gap displacement was measured using a digital dial indicator.

The blue curve of Figure 23 shows the measured force when increasing and decreasing the gap distance. It became apparent that the magnetic hysteresis effects were not negligible when a solid iron core was used. The red curve of Figure 23 shows the corresponding simulated force curve. Although the hysteresis effect was successfully included in the FEM model, the degree of hysteresis could not be matched to reality. Hysteresis was included in the FEM model by implementation of the 5-parameter Jiles-Atherton model [87,88]. Determining the correct parameter values is typically done by numerical methods, supported by measurements. In this thesis work the parameter space was manually explored to find suitable values to match simulations with measurements. A first guess was based on the values specified by Jiles et al. [87], valid for Fe-C 0.06 wt%. It is possible that the performed parameter search was insufficient to find suitable values. An investigation of additional or alternate sources of hysteresis was not performed and thus this possibility cannot be entirely discarded.

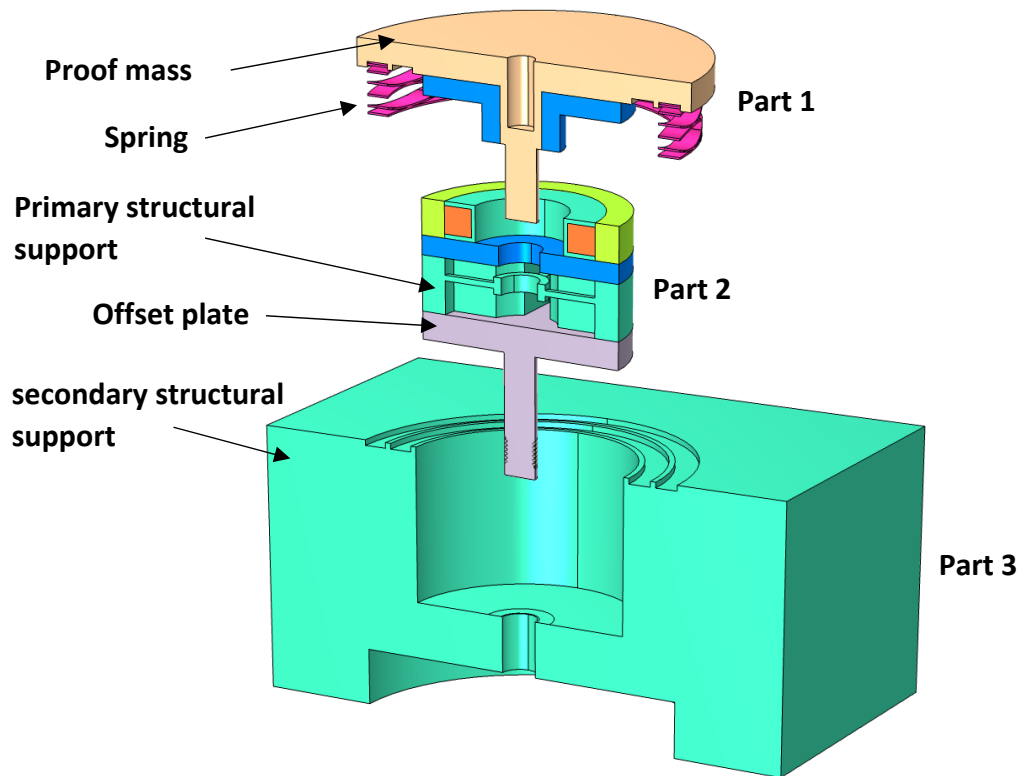


Figure 21. Exploded diagram of prototype. Top: Part 1 consisting of proof mass, spring and core component. Middle: Part 2 consisting of magnet, coil, core component, offset plate and support structure. Bottom: Part 3 is used as support structure.

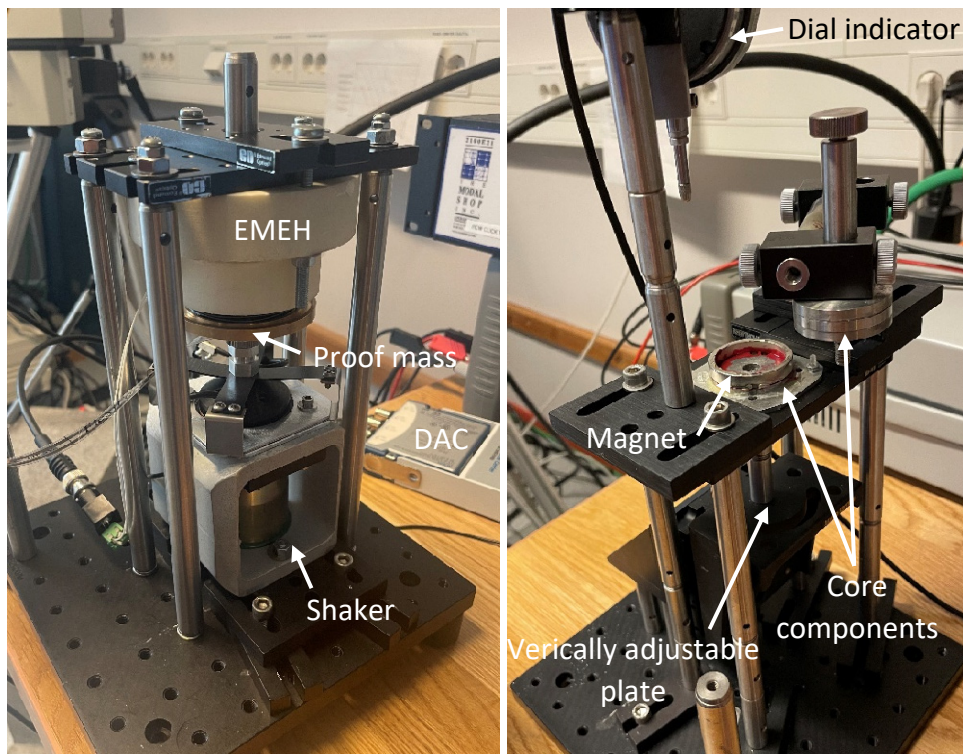


Figure 22. Left: A shaker excites the EMEH by applying a harmonically oscillating force directly on the proof mass. Right: Setup to measure gap force at varying gap distance. Only the force due to magnetic flux in the airgap is measured, i.e., no spring.

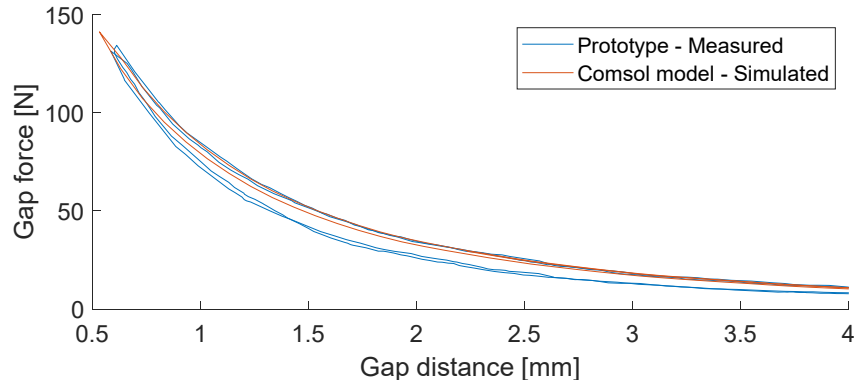


Figure 23. Gap force resulting from magnetic flux in the air gap (i.e., spring is not included). Measured (blue) and simulated (red) gap force. Top part of hysteresis curve corresponds to increasing the gap distance.

Taking into account the discrepancy in hysteresis, the results of paper I were able to match the frequency dependent behavior, regarding resonance shift and peak power trend, between measurement and simulation. Material parameters described in literature, for a laminated iron core, were then applied to the FEM model, resulting in a negligible hysteresis for the system. This allowed for a tuning to significantly lower frequencies, down to 20 Hz as shown in Figure 24. Figure 25 shows the model with spring offset tuned to give a resonance at 40 Hz, using a harmonic force excitation of amplitude 70 mN (corresponding to an excitation acceleration of approx. 0.039g).

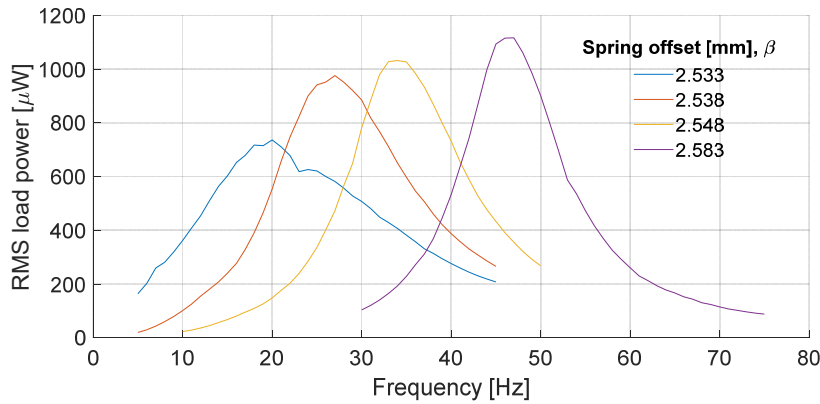


Figure 24. Simulated load power using the low hysteresis model.

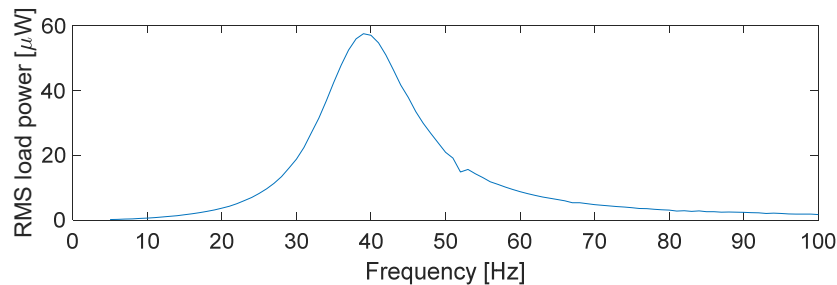


Figure 25. Frequency response using parameterization tuned to 40Hz.

The final step to determine the potential performance of the VEH was then to run the FEM simulation using accelerometer data as input for excitation. The accelerometer data is shown in Figure 26 and the resulting power output from the VEH is shown in Figure 27.

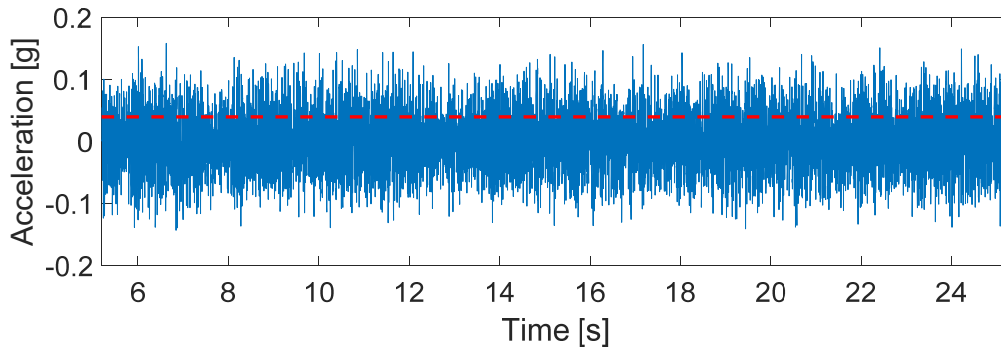


Figure 26. In situ measured vibrational acceleration data from automotive source, driving on a highway at ~ 70 km/h. Dotted red line shows the mean of the acceleration magnitude at 0.039 g

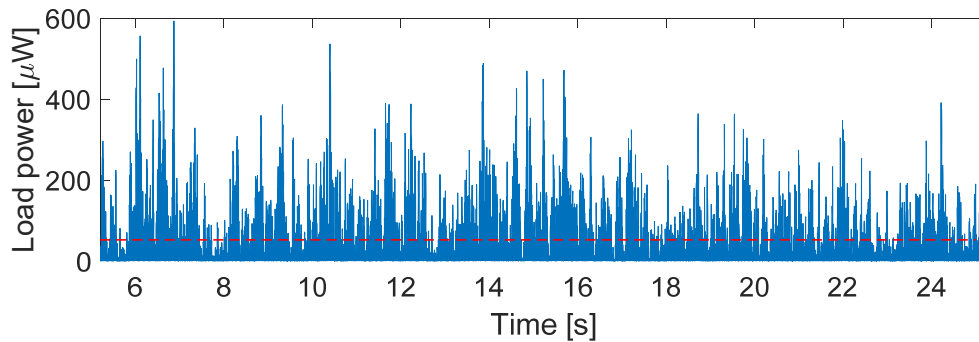


Figure 27. Simulated load power using measured vibration data as input. Dotted red line shows the mean power of $52\text{ }\mu\text{W}$.

The EMEH concept and design for belt buckle vibration harvesting shows promising results regarding generated output power for safety sensors in modern automotive vehicles. The results show the potential to generate useful amounts of power ($52\text{ }\mu\text{W}$) when harvesting energy in-car during normal road conditions at ~ 70 km/h, without making use of any dynamic tuning. Although the full frequency tuning potential is not explored, it is shown that the tuning range of a single device is at least 20 Hz to 45 Hz, a useful range considering typical in-car vibrations. Considering the simplicity and robustness of the design, it could lead to a competitive alternative for use not only in an automotive application but also for other practical situations where only very small excitation signals exist such as in machinery or construction equipment.

4.1 Introduction to modelling of vibration energy harvesters

Creating a model to predict the behavior of a VEH system is useful for both development of VEH prototypes and probing the characteristics of the system. As the purpose of any VEH is to convert mechanical energy to electrical energy, it can always be described by work done in the mechanical domain and in the electrical domain, with an electromechanical coupling factor defining the energy transfer between domains.

Modeling of a physical system, be it mechanical or electrical can take the form of either lumped or distributed. The distributed model accounts for parameters distribution across the geometry of the system while the lumped model assumes each parameter can be characterized in a single point, or between two points. The cantilever beam PEH is a good example as both lumped and distributed mechanical models are used in literature. It is unlikely a distributed model for the mechanical domain would be warranted for an EMEH, unless it uses a flexible induction coil or the field generating material is flexible.

The lumped mechanical system of a cantilever VEH can be summarized by a free-body diagram, as shown in Figure 28 right. The diagram consists of mass, spring and dampeners. The mass should be taken as an effective mass, i.e., the effect of the distributed mass yet acting only on the beam tip. The spring acts as a force restoring the beam tip to equilibrium and the dampeners retard movement of the tip.

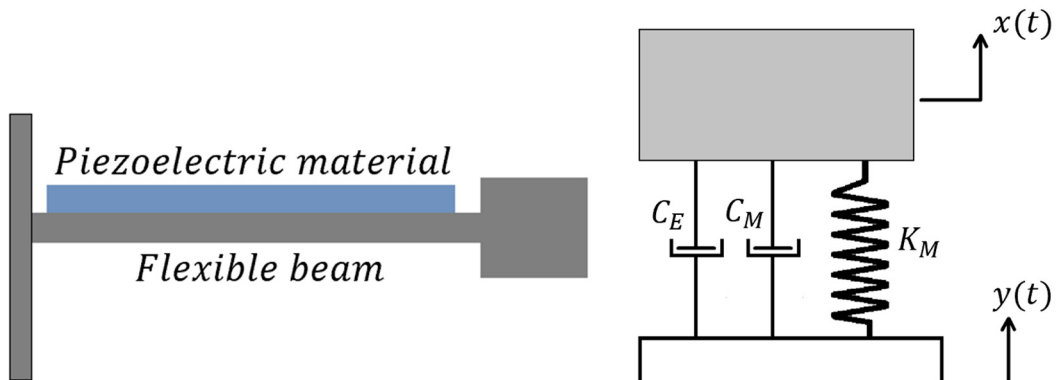


Figure 28. Representation of PEH (right) with a corresponding free body diagram (left). C_E and C_M are the electrical and mechanical damping coefficients. k_M is the mechanical spring coefficient. m is the effective mass of the system. $x(t)$ is the proof mass or tip displacement and $y(t)$ is the base displacement.

For a clamped-free beam with base excitation $y(t)$, the displacement $x(t)$ of the beam tip is given by Equation (11). Mechanical damping and stiffness are given by C_M and K_M , both assuming no effects from the electromechanical coupling, m is the effective mass and f is the electrical damping force.

$$m\ddot{x} + C_M\dot{x} + K_Mx + f = m\ddot{y} \quad (11)$$

The electrical domain is described by the lumped element model of Figure 29. The piezoelectric layer is here modeled as a current source, i , in parallel with a capacitance, C_P , and resistance, R_P . The capacitance is a result of the electrode separated by a thin dielectric. The resistance is a result of the resistivity of the system. Kirchhoff's law can then be used to derive Equation (12).

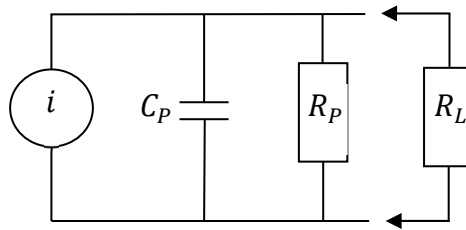


Figure 29. Lumped element model of electrical domain for a PEH. C_P , R_P , R_L are the capacitance, resistance due to PEH resistivity and load resistance. i is the generated current.

$$i = C_P\dot{v} + \frac{v}{R_L} + \frac{v}{R_P} \quad (12)$$

The distributed bending behavior of a beam was well established by the beginning of the 1900s, resulting in e.g., the Timoshenko–Ehrenfest beam theory [89]. A simpler form, which is commonly used today and referred to as Euler-Bernoulli beam theory, was derived by Daniel Bernoulli and Leonard Euler and published in 1744 [90,91]. This theory states that the relationship governing the one-dimensional bending shape in a beam is given by Equations (13) and (14):

$$M = -EI \frac{d^2\omega}{dx^2} \quad (13)$$

$$\frac{d^2}{dx^2} \left[EI \frac{d^2\omega}{dx^2} \right] = p \quad (14)$$

Where ω is the beam deflection at a point x , p is the applied force, E is the elastic modulus, I is the second moment of area of the beam's cross section and M is the bending moment. Some assumptions within this theory are; the beam deflection is small, the load is only lateral and shear deformation and rotatory inertia can be ignored [89].

The equation of motion based on the distributed model has the same form as the lumped model, but uses the distributed forces as derived by Euler Bernoulli beam theory. The sum of forces is in this case given by Equation (15), where c_s is the internal viscoelastic damping, c_a

is the air damping, m is the mass per unit length, ω_b is the base displacement and ω_{rel} is the beam displacement relative the base [92,93]. The effect of the beam's mechanical stiffness and the electrical damping is included in $M(x, t)$. Mechanical damping effects are included as a strain-rate damping, due to internal friction, and viscous air damping.

$$\frac{\partial^2 M(x, t)}{\partial x^2} + c_s I \frac{\partial^5 \omega_{rel}(x, t)}{\partial x^4 \partial t} + c_a \frac{\partial \omega_{rel}(x, t)}{\partial t} + m \frac{\partial^2 \omega_{rel}(x, t)}{\partial t^2} = m \frac{\partial^2 \omega_b(x, t)}{\partial t^2} - c_a \frac{\partial \omega_b(x, t)}{\partial t} \quad (15)$$

The circuit equation is identical to the lumped case. The PEH current can now be derived using the piezoelectric constitutive equations together with the Euler-Bernoulli beam theory [92], resulting in Equation (16). d_{31} is the piezoelectric constant, Y_p is the young's modulus of the PZT material, h_{pc} is the thickness of the PZT layer, b is the width of the beam and L is the length of beam.

$$C_p \frac{dv(t)}{dt} + \frac{v(t)}{R_L} = - \int_{x=0}^L d_{31} Y_p h_{pc} b \frac{\partial^3 \omega_{rel}(x, t)}{\partial x^2 \partial t} \quad (16)$$

There are additional methods to model a VEH, such as Finite Element modeling or with a circuit equivalent model.

A sub-field of research in VEH modeling is unified modeling of VEH's. The lumped model for the mechanical domain can be the same for different types of VEH. As an example, a magnet attached to a base by a spring, oscillating within a coil (see Figure 30) is described by the same free-body diagram as in Figure 28 left. By a suitable choice of dimensionless variables, both PEH and EMEH power performance can be expressed in the same way. Analysis of such a unified model can highlight the strengths and weaknesses of different types of VEH. It can also provide a useful tool to be used in the development of prototype VEH's.

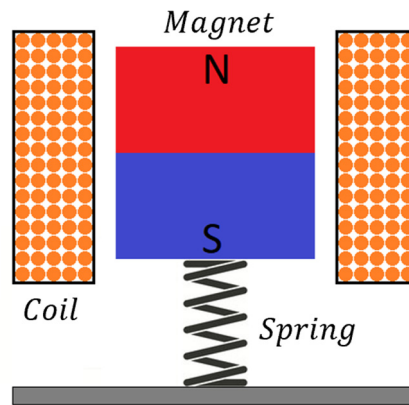


Figure 30. Representation of an EMEH.

4.2 Analysis of a unified model for vibration energy harvetsters

In paper II, the derivation of such a unified model is given for the case of PEH and EMEH. To further probe the system characteristics, both harmonic base excitation and a prescribed displacement are considered. The optimal values of power, load resistance and excitation frequency, in dimensionless form, are explored in the space of normalized quality factor, k ,

and normalized internal resistance, ξ_E . The internal resistance here refers either R_P as defined in Figure 29 or R_W as defined in Figure 31. The expressions for the dimensionless parameters are given in Table 4. ω_N is here the natural frequency of the VEH. R_P , R_W , R_L , C_P and L are describe in Figure 29 and Figure 31. Q_{crit} is the mechanical quality factor at which the system, under resonance, reaches a theoretical maximum in output power [94].

Table 4. Dimensionless parameters.

Parameter	Expression	Name
k	Q/Q_{crit}	Normalized quality factor
γ	ω/ω_N	Normalized angular excitation frequency
ξ_C	PEH: $1/R_L\omega_N C_P$ EMEH: $R_L/\omega_N L$	Normalized load resistance
ξ_E	PEH: $1/R_P\omega_N C_P$ EMEH: $R_W/\omega_N L$	Normalized internal resistance

The model in paper II is derived from Equation (11) and the lumped element models for a PEH and EMEH (see Figure 29 and Figure 31 and Equations (12) and (17)).

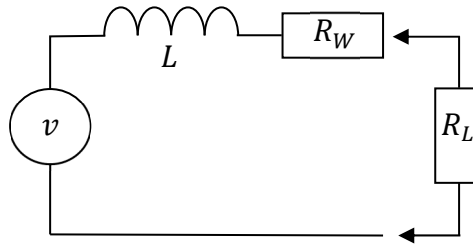


Figure 31. Lumped element model of electrical domain for an EMEH. L , R_W , R_L are the coil inductance, coil resistance and load resistance. v is the generated voltage.

$$v = L \frac{di}{dt} + (R_W + R_L)i \quad (17)$$

Based on these sets of equations, the relationship between the mechanical and electrical parameters can theoretically be analytically solved in the frequency domain under the assumption of harmonic signals. In practice however, the complexity of the problem, taking into account all parameters, seems to prohibit a solution to be found. This is typically not an issue in most literature, where at least one parameter is deemed insignificant. As an example, the internal resistance could be assumed as much smaller or larger than the load resistance and, depending on the VEH type, could then be excluded from the model without significant effect on the model accuracy. This can be applicable for certain load cases and when dealing with a certain type of VEH, but a unified model without a defined load (other than that it is purely resistive) cannot make these assumptions. Thus, the analytical solution can only be taken so far before numerical methods need to be implemented.

The locally optimal values of dimensionless excitation frequency, γ , and dimensionless load resistance, ξ_C , can be found by finding the intersections of solutions to $\partial \bar{P}_{IL} / \partial \xi_C = 0$ and $\partial \bar{P}_{IL} / \partial \gamma = 0$. A numerical method for solving this problem can be derived from the following requirement:

A value of ξ_C lies in the intersection to the solutions to $\partial \bar{P}_{IL} / \partial \xi_C = 0$ and $\partial \bar{P}_{IL} / \partial \gamma = 0$ if this value, input to solution for $\partial \bar{P}_{IL} / \partial \gamma = 0$, generates a value of γ that when input to the solution for $\partial \bar{P}_{IL} / \partial \xi_C = 0$ generates again the initial input value of ξ_C .

To numerically find all the values of ξ_C which fullfill this requirement a $M \times N$ data set is defined, corresponding to all the descrete combinations of ξ_C and ξ_E in a chosen range, where M and N are the number of descrete values for each parameter. For a set value of k , which will be incremented in small steps, the analytical solution to $\partial \bar{P}_{IL} / \partial \gamma = 0$ is used to acquire the $M \times N$ numerical values for optimal γ . The numerical output of γ_{opt} in then used as input to the analytical solution to $\partial \bar{P}_{IL} / \partial \xi_C = 0$. The numerical computation then consists of finding the zeros of $\xi_C - \xi_{C_{opt}}$. A linear fit is used to find the near-zero crossings. The above algorithm is performed over a range of k -values, resulting in the power optimal values of γ and ξ_C in the space of k vs ξ_E .

There exists a certain relationship between ξ_E and k where, for small values of ξ_E or large values of k , there are three zeros in $\xi_C - \xi_{C_{opt}}$. Figure 31 left shows this region for the case of $k = 1.1$ and Figure 31 right shows the lack of such a region for $k = 0.9$. One of the three solutions correspond to a local minimum in power. The other two corresponds to the systems resonance and anti-resonance states (as described earlier in section 1.4.1). The numerical analysis can thus show the relationship between quality factor and intrinsic resistance at which a VEH system will exhibit anti-resonance. In Figure 33 this boundary is dubbed k_{crit} and is expressed in dimensionless parameters.

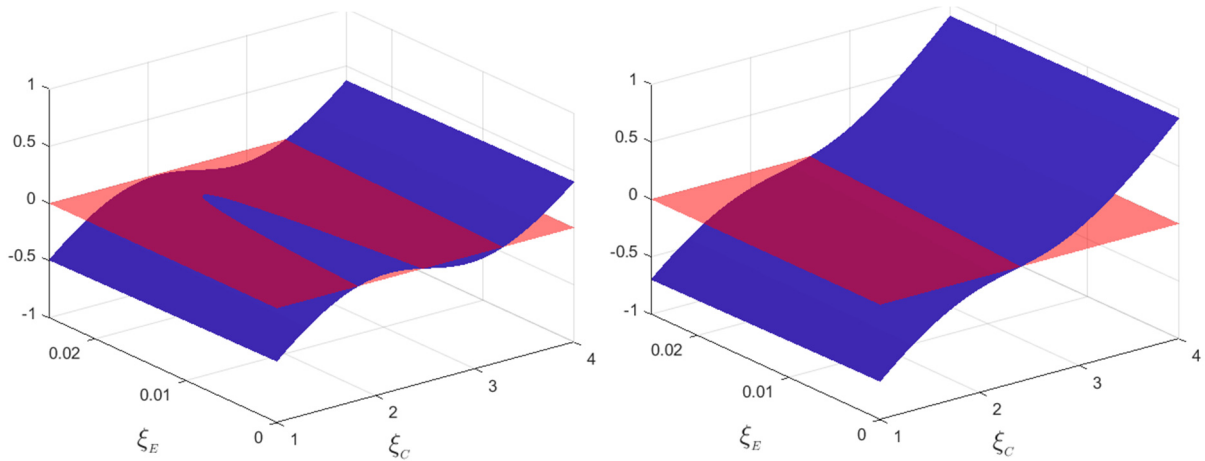


Figure 32. Surfaces of $\xi_C - \xi_{C_{opt}}$ in blue with the zero-plane in red. Left: $k = 1.1$. Right: $k = 0.9$.

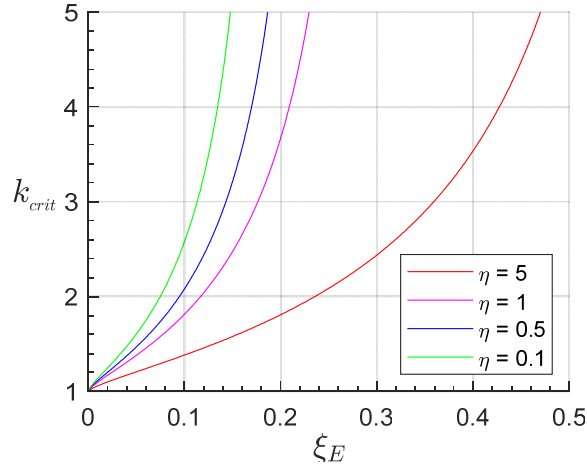


Figure 33. Minimum value of k required for the existence of an anti-resonant solution. $\eta = \{0.1, 0.5, 1, 5\}$, from left to right.

The raw output from the numerical calculations described above are the surfaces, in k - ξ_E space, for the power optimal values of γ and ξ_C as well as the values of optimal power and efficiency in the same space. Analyzing these surfaces can provide a clearer picture of the behavior of VEH systems and result in new insights. From Figure 34 we can see the region where the typical assumption, that resonance occurs at the natural frequency, is true. We can see that the resonance frequency tends towards the natural frequency at large k and the anti-resonant frequency towards $\sqrt{1 + \eta}$ (if $\eta = 1$ then this value is 1.41).

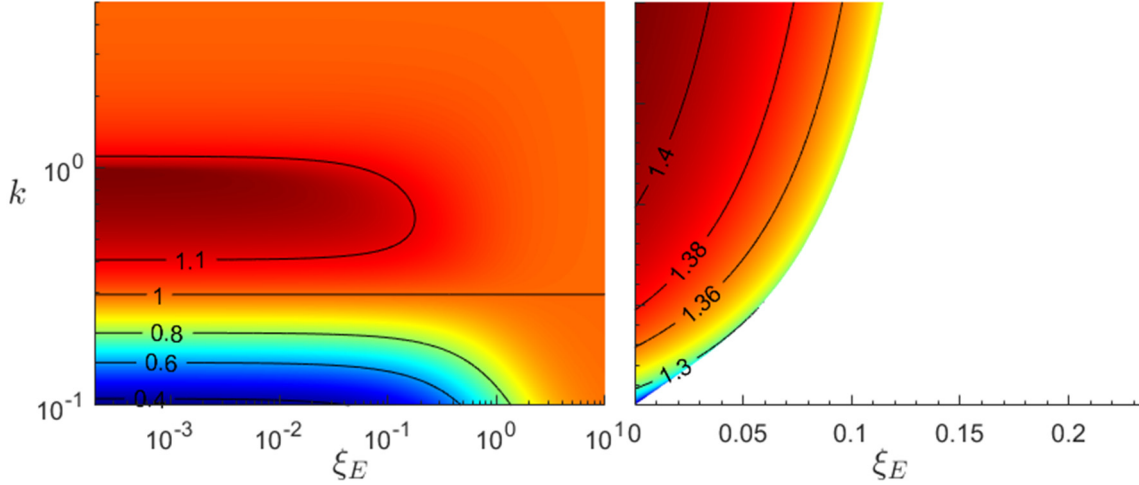


Figure 34. Normalized angular excitation frequency under the condition of power optimal load and $\eta = 1$. Left: at resonance. Right: at anti-resonance. The color scale is linear and independent for each plot

Assuming we can design an arbitrary EMEH or PEH to operate either at the resonant or the anti-resonant state, the two VEH systems will benefit differently from operating under either condition. From the numerical results we can compare these states regarding the key performance parameters: output voltage, power and efficiency

As described earlier, in section 1.2, a VEH system will in general include circuitry for rectification of the generated signal. The diodes typically used in such circuitry can have a

substantial voltage drop across them (ranging between approximately 0.2V to 0.7V depending on the type of diode). Luckily this voltage drop is absolute and the larger the output voltage from the VEH the smaller the proportion of power is lost in the diodes. Due to the series nature of the EMEH circuit model, a large output voltage is obtained when ξ_C is large and ξ_E is small, while for a PEH both should be small. From the results in Figure 36 left and Figure 35 we can see that a system run at resonance can in general achieve large values of optimal ξ_C at high k values. On the contrary, values of optimal $\xi_C \ll 1$ at resonance require large values of η and $k \ll 1$. Only at anti-resonance (see Figure 36 right) can we achieve an optimal $\xi_C \ll 1$ at small values of η . In both cases (PEH/EMEH) an increasingly beneficial value of optimal ξ_C , with regards to output voltage, is achieved at increasing k . In a similar sense, the power characteristics at anti-resonance (Figure 37 right) also favor the PEH over the EMEH as the power rapidly declines at increasing ξ_E and k , while it is close to its theoretical maximum for $\xi_E \ll 1$, regardless of k .

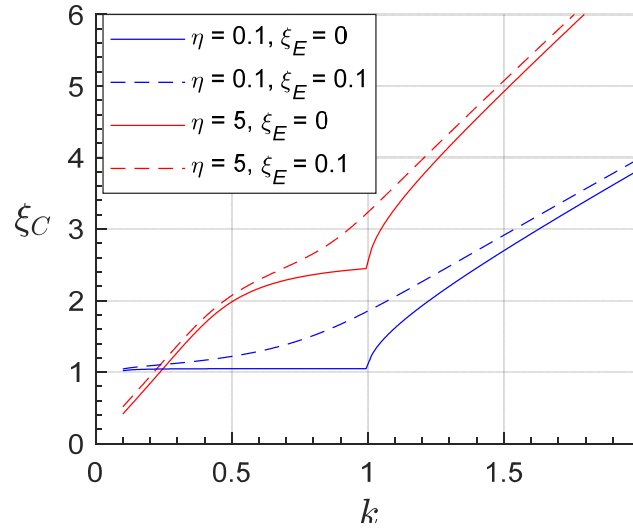


Figure 35. Optimum normalized load resistance, at resonant excitation frequency. $\eta = \{5, 1\}$ and $\xi_E = \{0, 0.1\}$

Looking to Table 4 we can see that the practical design parameters available, for manipulating ξ_C and ξ_E are ω_N , C_P , L , R_W , R_P and R_L . Spring stiffness and mass determines ω_N , which for a cantilever beam with proof mass is determined by beam width, thickness, Young's modulus and proof mass weight. Electrode area, electrode separation and dielectric material properties determine both C_P and R_P . Coil geometry (length and area) and number of windings determine L for an air wound coil. Coil wire length and conductivity determine R_W . R_L is determined by the load electronics. Based on the argument from the previous paragraph and assuming the PEH is limited to small η , the parameters ω_N , C_P , R_P and R_L should all be maximized for the PEH. For the EMEH, ω_N , L and R_W should be minimized while R_L is maximized. As mentioned in the previous paragraph, a high k -value is beneficial with regards to power output and voltage (at resonance and anti-resonance). The parameter k is a function of ω_N and η as well as mass and mechanical damping. Due to the overlap between the parameters ξ_C , ξ_E , η and k , finding the optimal geometry and material properties, while adhering to the power optimal proportionalities, is a complex task for both types of VEH.

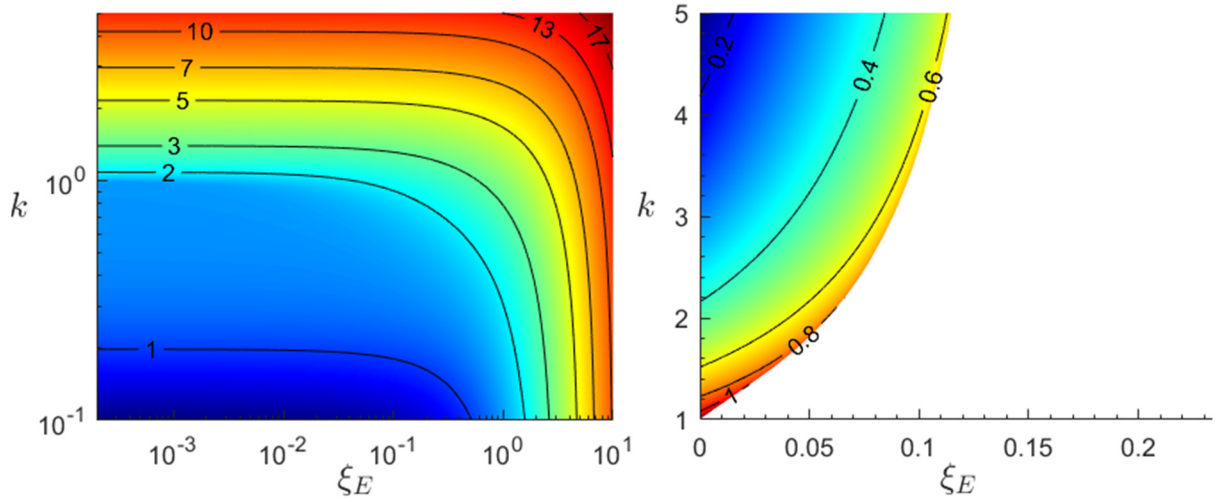


Figure 36. Power optimum normalized load resistance for $\eta = 1$. Left: at resonance. Right: at anti-resonance. The color scale is logarithmic and independent for each plot

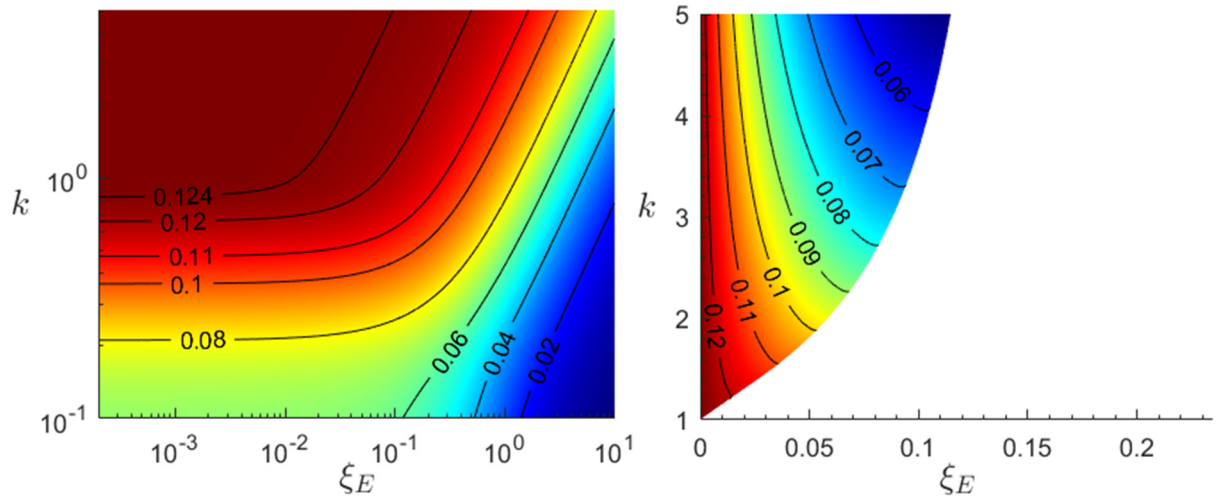


Figure 37. Dimensionless power at optimal load and $\eta = 1$. Left: at resonance. Right: at anti-resonance. The color scale is linear and independent for each plot.

In the region of $k > 1$, in Figure 37, it can be derived that the dependance between the ratio k/ξ_E and value of \bar{P} to be traced follows a logarithmic slope. Figure 38 shows k/ξ_E as a function of \bar{P} at $\eta = \{5, 1, 0.1\}$. We can see that the sensitivity of k to ξ_E increases dramatically near the theoretical power maximum. The quality factor and/or effective coupling coefficient required to achieve a power output close to the theoretical maximum can thus become large for energy harvesters with large loss coefficient, such as for a typical EMEH.

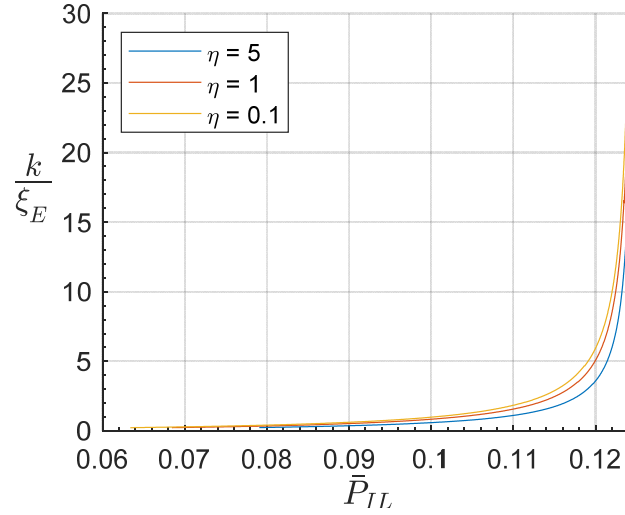


Figure 38. Sensitivity of k to ξ_E as a function of dimensionless power, i.e., the ratio of k to ξ_E when tracing a specific power value. This relationship only holds for $k > 1$.

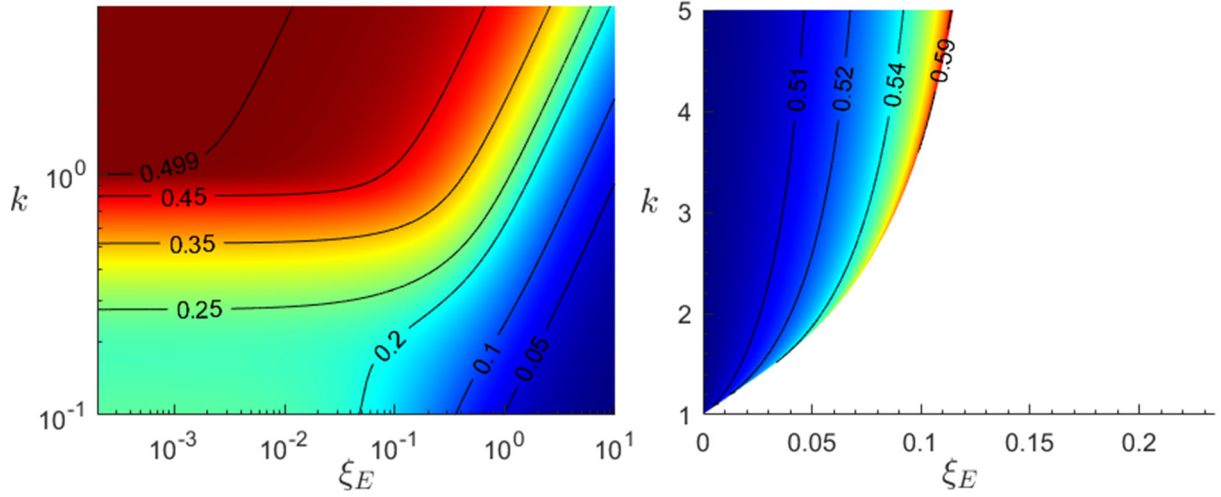


Figure 39. Power input to output efficiency under the condition of power optimal load and $\eta = 1$. Left: at resonance. Right: at anti-resonance. The color scale is linear and independent for each plot.

Assuming load resistance and excitation frequency remain optimized by load power, both VEH systems have a maximum efficiency of 50% at resonance (see Figure 39 left). At antiresonance the efficiency is above 50% (if $\xi_E > 0$) and increasingly so along the boundary of k_{crit} , in the direction of larger k and ξ_E (see Figure 39 right). It may be beneficial to operate in this region if the source power is small. If we instead assume an arbitrary γ and a load optimized by efficiency, the efficiency can approach 100%.

The primary results from modeling assuming a prescribed displacement lie in the validation of the expressions derived for the model with base excitation. The expressions for efficiency are equal in both cases, which is intuitive assuming efficiency is a purely intrinsic property. Optimal load resistance was also found to differ by only a term related to the electric damping, an effect negated by prescribed displacement.

To summarize, the results of this chapter help provide a clearer picture of VEH characteristics thanks to the detailed investigation of the effect from the resistive loss coefficient, under both resonance and anti-resonance. The numerical results described in this chapter take into account all the parameters of the unified lumped VEH model, under the condition of power optimal proportions, and thus a more complete picture is gained compared to previous literature which exclude one or more parameters. New insights gained from the analysis can be summarized as the following:

- The detailed effect of the intrinsic resistance on the critical coupling factor.
- The relationship between optimal load and intrinsic resistance favors the PEH at anti-resonance and the EMEH at resonance.
- The efficiency, under power optimal conditions, is potentially larger at anti-resonance.
- VEH systems with large intrinsic resistance reach a practical power limit before the theoretical limit.

5.1 Discussion and concluding remarks

The energy required by most small-scale electronics is insignificant next to the total energy of a moving vehicle. The possibility of wirelessly extracting a very small portion of this energy to enable wireless self-sufficient systems is an attractive and today proven concept. VEH to date utilize three main areas of power extraction; tire surface buckling, suspension compression and ambient vibrations. The energy available from additional electrical damping in the suspension is by a wide margin the largest. This is due to that VEH can be strongly coupled to the total oscillating mass of the vehicle. This source of energy is naturally limited to suspension units. Sources of ambient vibrational energy are available throughout the vehicle, the downside being most of these sources are already significantly damped (perhaps excluding those in direct connection with the engine). Areas close to the passenger seats likely have the least ambient vibrations, to optimize the user experience.

This thesis describes two energy harvesters for scavenging ambient vibrations within a vehicle, one utilizing piezoelectricity and the other magnet induction. The described PEH placed on the flexplate likely has a larger source of power compared to the EMEH on belt-buckle, naturally leading to more harvested power. The described PEH is an example of a VEH utilizing the environment, centrifugal force and gravitational pull in this case, to boost the output performance and reduce required size. The relatively static environment, with very small vibrations, on the belt-buckle puts a high demand on performance. There is also a neutral size limit. A VEH larger than the belt-buckle would likely be deemed bulky. The described macroscale EMEH has a simple design but still manages a large power density and a usable power output if intermittent communication can be accepted. The low-level vibration capabilities make this EMEH a likely competitive VEH in many other areas of the vehicle.

The market trend towards an increasing number of purely electric vehicles may put additional requirements for ambient vibration VEH in vehicles. E.g., with no combustion engine a significant source of vibration is gone. The current limitation in travel range of electrical vehicles has likely put a strict requirement on energy management and weight minimization. Thus, the additional weight and energy consumption due to a VEH needs to be well justified. Safety sensors may have additional requirements inhibiting the use of a VEH as sole power source.

Which type of transduction mechanism to choose can be a difficult choice as successful attempts to mitigate the weaknesses of each can be found in most research areas. The

solutions can be more or less complex, and it can therefore still be of interest to explore the pros and cons of the basics VEH systems. Unified modeling of VEHs provides a tool for such an analysis. Although such a model can highlight useful characteristics the unified aspect creates the need for a simplified lumped model. E.g., the strain distribution in the piezoelectric layer is a key parameter which is lost in the lumped model. The unified model described in paper II requires the use of numerical methods. A complete analytical expression would be of more use.

Surveying the research field of vibrational energy harvesting in vehicles we find that there are several regions where a VEH can be of use. The stochastic resonance PEH described here shows potential for an efficient VEH in a rotational environment. The demonstrated use of VEHs for ambient vibrations in the passenger/driver area is missing in literature. The EMEH described here shows the potential implementation of such a VEH.

5.2 Future work

Of the two VEHs for ambient vehicle vibrations, described in this thesis, none are rigorously optimized and thus this work needs to be performed to determine their true potential. In both cases an improved experimental test setup would be beneficial for system characterization and optimization.

The analysis of the unified model could be expanded to include more transduction mechanisms, as these only differ in the electrical domain when using the lumped approach. An attempt could be made to include corrections factors considering the approximations of the lumped model. The analytical results would benefit from a rigorous validation by lab measurements or measurement data from literature (if all necessary data can be extrapolated).

The possibility of utilizing the magnetostriction effect for an improved VEH in the belt-buckle environment will be examined and an energy harvester to extract the relatively large biomechanical energy of a passenger buckling in/out will be developed.

-
- [1] Harold I. Sharlin. From Faraday to the Dynamo. *Sci Am* 1961;204:107–19.
- [2] Smith GS. Faraday’s first dynamo: A retrospective. *Am J Phys* 2013;81:907–17. <https://doi.org/10.1119/1.4825232>.
- [3] Algave É, Boulard J, Sloane TO, Lungren CM. The electric light : its history, production, and applications. New York: D. Appleton and Co.; 1884.
- [4] Weisbrich M, Blume H, Paya-Vaya G. A Silicon-Proof Controller System for Flexible Ultra-Low-Power Energy Harvesting Platforms. 2022 11th International Conference on Modern Circuits and Systems Technologies (MOCASST), IEEE; 2022, p. 1–6. <https://doi.org/10.1109/MOCASST54814.2022.9837540>.
- [5] Kopta V, Enz C. Ultra-Low Power FM-UWB Transceivers for IoT. River Publishers; 2019.
- [6] Schumacher T, Stadelmayer M, Faseth T, Pretl H. A Review of Ultra-Low-Power and Low-Cost Transceiver Design. 2017 Austrochip Workshop on Microelectronics (Austrochip), IEEE; 2017, p. 29–34. <https://doi.org/10.1109/Austrochip.2017.15>.
- [7] Jahan MS, Langford J, Holleman J. A low-power FSK/OOK transmitter for 915 MHz ISM band. 2015 IEEE Radio Frequency Integrated Circuits Symposium (RFIC), IEEE; 2015, p. 163–6. <https://doi.org/10.1109/RFIC.2015.7337730>.
- [8] Kopta V, Enz CC. A 4-GHz Low-Power, Multi-User Approximate Zero-IF FM-UWB Transceiver for IoT. *IEEE J Solid-State Circuits* 2019;54:2462–74. <https://doi.org/10.1109/JSSC.2019.2917837>.
- [9] Bai Y, Jantunen H, Juuti J. Energy Harvesting Research: The Road from Single Source to Multisource. *Advanced Materials* 2018;30:1707271. <https://doi.org/10.1002/adma.201707271>.
- [10] Maurya D, Kumar P, Khaleghian S, Sriramdas R, Kang MG, Kishore RA, et al. Energy harvesting and strain sensing in smart tire for next generation autonomous vehicles. *Appl Energy* 2018;232. <https://doi.org/10.1016/j.apenergy.2018.09.183>.
- [11] Mondal S, Wijewardena K, Karrauswami S, Kumar D, Chahal P, Ghannam M, et al. A Wireless Battery-less Seat Sensor for Autonomous Vehicles. 2020 IEEE 70th Electronic Components and Technology Conference (ECTC), IEEE; 2020. <https://doi.org/10.1109/ECTC32862.2020.00357>.
- [12] Rui X, Zeng Z, Zhang Y, Li Y, Feng H, Huang X, et al. Design and Experimental Investigation of a Self-Tuning Piezoelectric Energy Harvesting System for Intelligent

- Vehicle Wheels. *IEEE Trans Veh Technol* 2020;69.
<https://doi.org/10.1109/TVT.2019.2959616>.
- [13] Zhu D, Wang L, Henaut J, Beeby S. Comparisons of Energy Sources for Autonomous In-car Wireless Tags for Asset Tracking and Parking Applications. *Procedia Eng* 2014;87:783–6. <https://doi.org/10.1016/j.proeng.2014.11.680>.
 - [14] Lee JH, Jeong K, Lee J, Yoo S, Lee B, Ha J, et al. Development of Adaptive Powertrain Control Utilizing ADAS and GPS, 2019. <https://doi.org/10.4271/2019-01-0883>.
 - [15] Sivertsson M, Sundström C, Eriksson L. Adaptive Control of a Hybrid Powertrain with Map-based ECMS. *IFAC Proceedings Volumes* 2011;44:2949–54.
<https://doi.org/10.3182/20110828-6-IT-1002.02091>.
 - [16] Guerrero-Ibáñez J, Zeadally S, Contreras-Castillo J. Sensor Technologies for Intelligent Transportation Systems. *Sensors* 2018;18:1212. <https://doi.org/10.3390/s18041212>.
 - [17] Abdelkareem MAA, Xu L, Ali MKA, Elagouz A, Mi J, Guo S, et al. Vibration energy harvesting in automotive suspension system: A detailed review. *Appl Energy* 2018;229:672–99. <https://doi.org/10.1016/j.apenergy.2018.08.030>.
 - [18] Chilabi HJ, Salleh H, Al-Ashtari W, Supeni EE, Abdullah LC, As'array AB, et al. Rotational Piezoelectric Energy Harvesting: A Comprehensive Review on Excitation Elements, Designs, and Performances. *Energies (Basel)* 2021;14:3098.
<https://doi.org/10.3390/en14113098>.
 - [19] Gao X, Wu J, Yu Y, Dong S. A modified barbell-shaped PNN-PZT-PIN piezoelectric ceramic energy harvester. *Appl Phys Lett* 2017;111:212904.
<https://doi.org/10.1063/1.5001803>.
 - [20] Koo B-G, Shin D-J, Lim D-H, Kim M-S, Kim I-S, Jeong S-J. Properties of Car-Embedded Vibrating Type Piezoelectric Harvesting System. *Applied Sciences* 2021;11:7449.
<https://doi.org/10.3390/app11167449>.
 - [21] Pepe G, Doria A, Roveri N, Carcaterra A. Vibration energy harvesting for cars: semi-active piezo controllers. *Archive of Applied Mechanics* 2022.
<https://doi.org/10.1007/s00419-022-02292-1>.
 - [22] Zhao Z, Wang T, Shi J, Zhang B, Zhang R, Li M, et al. Analysis and application of the piezoelectric energy harvester on light electric logistics vehicle suspension systems. *Energy Sci Eng* 2019;7:2741–55. <https://doi.org/10.1002/ese3.456>.
 - [23] Zhao Z, Wang T, Zhang B, Shi J. Energy Harvesting from Vehicle Suspension System by Piezoelectric Harvester. *Math Probl Eng* 2019;2019:1–10.
<https://doi.org/10.1155/2019/1086983>.
 - [24] Alhumaid S, Hess D, Guldiken R. A Noncontact Magneto–Piezo Harvester-Based Vehicle Regenerative Suspension System: An Experimental Study. *Energies (Basel)* 2022;15:4476. <https://doi.org/10.3390/en15124476>.

- [25] Zhou R, Yan M, Sun F, Jin J, Li Q, Xu F, et al. Experimental validations of a magnetic energy-harvesting suspension and its potential application for self-powered sensing. *Energy* 2022;239:122205. <https://doi.org/10.1016/j.energy.2021.122205>.
- [26] Esmaeeli R, Aliniagerdroudbari H, Hashemi SR, Alhadri M, Zakri W, Batur C, et al. Design, modeling, and analysis of a high performance piezoelectric energy harvester for intelligent tires. *Int J Energy Res* 2019;43:5199–212. <https://doi.org/10.1002/er.4441>.
- [27] Seo J, Jhang K-Y, Lee H, Kim Y-C. Vibration energy harvesting technology for smart tire monitoring. *Journal of Mechanical Science and Technology* 2019;33:3725–32. <https://doi.org/10.1007/s12206-019-0714-2>.
- [28] Miao G, Fang S, Wang S, Zhou S. A low-frequency rotational electromagnetic energy harvester using a magnetic plucking mechanism. *Appl Energy* 2022;305:117838. <https://doi.org/10.1016/j.apenergy.2021.117838>.
- [29] Paul K, Amann A, Roy S. Tapered nonlinear vibration energy harvester for powering Internet of Things. *Appl Energy* 2021;283:116267. <https://doi.org/10.1016/j.apenergy.2020.116267>.
- [30] Aktakka EE, Najafi K. A Micro Inertial Energy Harvesting Platform With Self-Supplied Power Management Circuit for Autonomous Wireless Sensor Nodes. *IEEE J Solid-State Circuits* 2014;49:2017–29. <https://doi.org/10.1109/JSSC.2014.2331953>.
- [31] Kasargod PS, Rashidzadeh R, Ahmadi M. A MEMS based rectifier for energy harvesting. 2017 European Conference on Circuit Theory and Design (ECCTD), IEEE; 2017, p. 1–4. <https://doi.org/10.1109/ECCTD.2017.8093296>.
- [32] Staaf LGH, Lundgren P, Enoksson P. Present and future supercapacitor carbon electrode materials for improved energy storage used in intelligent wireless sensor systems. *Nano Energy* 2014;9:128–41. <https://doi.org/10.1016/j.nanoen.2014.06.028>.
- [33] Pender JP, Jha G, Youn DH, Ziegler JM, Andoni I, Choi EJ, et al. Electrode Degradation in Lithium-Ion Batteries. *ACS Nano* 2020;14:1243–95. <https://doi.org/10.1021/acsnano.9b04365>.
- [34] Narita F, Fox M. A Review on Piezoelectric, Magnetostrictive, and Magnetoelectric Materials and Device Technologies for Energy Harvesting Applications. *Adv Eng Mater* 2018;20. <https://doi.org/10.1002/adem.201700743>.
- [35] Apicella V, Clemente CS, Davino D, Leone D, Visone C. Review of Modeling and Control of Magnetostrictive Actuators. *Actuators* 2019;8. <https://doi.org/10.3390/act8020045>.
- [36] Bjurström J, Ohlsson F, Rusu C, Johansson C. Unified Modeling and Analysis of Vibration Energy Harvesters under Inertial Loads and Prescribed Displacements. *Applied Sciences* 2022;12:9815. <https://doi.org/10.3390/app12199815>.

- [37] Wang ZL. Triboelectric Nanogenerators as New Energy Technology for Self-Powered Systems and as Active Mechanical and Chemical Sensors. *ACS Nano* 2013;7:9533–57. <https://doi.org/10.1021/nn404614z>.
- [38] Boisseau S, Despesse G, Ahmed B. Electrostatic Conversion for Vibration Energy Harvesting. *Small-Scale Energy Harvesting, InTech*; 2012. <https://doi.org/10.5772/51360>.
- [39] Tang G, Cheng F, Hu X, Huang B, Xu B, Li Z, et al. A Two-Degree-of-Freedom Cantilever-Based Vibration Triboelectric Nanogenerator for Low-Frequency and Broadband Operation. *Electronics (Basel)* 2019;8:1526. <https://doi.org/10.3390/electronics8121526>.
- [40] Halvorsen E, Nguyen SD. MEMS Electrostatic Energy Harvesters with Nonlinear Springs. *Advances in Energy Harvesting Methods*, New York, NY: Springer New York; 2013, p. 63–90. https://doi.org/10.1007/978-1-4614-5705-3_3.
- [41] Harne RL, Wang KW. A review of the recent research on vibration energy harvesting via bistable systems. *Smart Mater Struct* 2013;22:023001. <https://doi.org/10.1088/0964-1726/22/2/023001>.
- [42] Halim MA, Kim DH, Park JY. Low Frequency Vibration Energy Harvester Using Stopper-Engaged Dynamic Magnifier for Increased Power and Wide Bandwidth. *Journal of Electrical Engineering and Technology* 2016;11. <https://doi.org/10.5370/JEET.2016.11.3.707>.
- [43] Tri Nguyen H, Genov DA, Bardaweel H. Vibration energy harvesting using magnetic spring based nonlinear oscillators: Design strategies and insights. *Appl Energy* 2020;269. <https://doi.org/10.1016/j.apenergy.2020.115102>.
- [44] Pertin O, Guha K, Jakšić O, Jakšić Z, Iannacci J. Investigation of Nonlinear Piezoelectric Energy Harvester for Low-Frequency and Wideband Applications. *Micromachines (Basel)* 2022;13:1399. <https://doi.org/10.3390/mi13091399>.
- [45] Ghandchi Tehrani M, Elliott SJ. Extending the dynamic range of an energy harvester using nonlinear damping. *J Sound Vib* 2014;333. <https://doi.org/10.1016/j.jsv.2013.09.035>.
- [46] Colin M, Basrour S, Rufer L, Bantignies C, Nguyen-Dinh A. Highly Efficient Low-frequency Energy Harvester Using Bulk Piezoelectric Ceramics. *J Phys Conf Ser* 2013;476:012133. <https://doi.org/10.1088/1742-6596/476/1/012133>.
- [47] IEEE Standard on Piezoelectricity. *ANSI/IEEE Std 176-1987* 1988:0_1.
- [48] Priya S, Inman DJ, editors. *Energy Harvesting Technologies*. Boston, MA: Springer US; 2009. <https://doi.org/10.1007/978-0-387-76464-1>.
- [49] Rajasekar S, Sanjuan MAF. *Nonlinear Resonances*. Cham: Springer International Publishing; 2016. <https://doi.org/10.1007/978-3-319-24886-8>.

- [50] Ando B, Baglio S, Bulsara AR, Marletta V. A Nonlinear Energy Harvester Operated in the Stochastic Resonance Regime for Signal Detection/Measurement Applications. *IEEE Trans Instrum Meas* 2020;69:5930–40. <https://doi.org/10.1109/TIM.2019.2957913>.
- [51] Brenes A, Morel A, Juillard J, Lefeuvre E, Badel A. Maximum power point of piezoelectric energy harvesters: a review of optimality condition for electrical tuning. *Smart Mater Struct* 2020;29:033001. <https://doi.org/10.1088/1361-665X/ab6484>.
- [52] KATZIR S. The Discovery of the Piezoelectric Effect. *Arch Hist Exact Sci* 2003;57:61–91. <https://doi.org/10.1007/s00407-002-0059-5>.
- [53] Fundamentals of Piezoelectricity. *Piezoelectric Transducers for Vibration Control and Damping*, London: Springer-Verlag; n.d., p. 9–35. https://doi.org/10.1007/1-84628-332-9_2.
- [54] Smith M, Kar-Narayan S. Piezoelectric polymers: theory, challenges and opportunities. *International Materials Reviews* 2022;67:65–88. <https://doi.org/10.1080/09506608.2021.1915935>.
- [55] Fraden J. *Handbook of Modern Sensors*. Cham: Springer International Publishing; 2016. <https://doi.org/10.1007/978-3-319-19303-8>.
- [56] Ballas RG. The Piezoelectric Effect – an Indispensable Solid State Effect for Contemporary Actuator and Sensor Technologies. *J Phys Conf Ser* 2021;1775:012012. <https://doi.org/10.1088/1742-6596/1775/1/012012>.
- [57] Safari A, Akdoğan EK, editors. *Piezoelectric and Acoustic Materials for Transducer Applications*. Boston, MA: Springer US; 2008. <https://doi.org/10.1007/978-0-387-76540-2>.
- [58] Pinin. Perovskite structure of PZT. Wikimedia Commons 2010.
- [59] Carpi F, editor. *Electromechanically Active Polymers*. Cham: Springer International Publishing; 2016. <https://doi.org/10.1007/978-3-319-31530-0>.
- [60] Jing-Feng Li. *Fundamentals of Piezoelectricity. Lead-Free Piezoelectric Materials*. first, WILEY; 2021.
- [61] Kim T, Ko Y, Yoo C, Choi B, Han S, Kim N. Design optimisation of wide-band piezoelectric energy harvesters for self-powered devices. *Energy Convers Manag* 2020;225:113443. <https://doi.org/10.1016/j.enconman.2020.113443>.
- [62] Bouhedma S, Rao Y, Schütz A, Yuan C, Hu S, Lange F, et al. System-Level Model and Simulation of a Frequency-Tunable Vibration Energy Harvester. *Micromachines (Basel)* 2020;11:91. <https://doi.org/10.3390/mi11010091>.
- [63] Jiang J, Liu S, Feng L, Zhao D. A Review of Piezoelectric Vibration Energy Harvesting with Magnetic Coupling Based on Different Structural Characteristics. *Micromachines (Basel)* 2021;12:436. <https://doi.org/10.3390/mi12040436>.

- [64] Sun S, Leng Y, Hur S, Sun F, Su X, Song H-C, et al. Energy Harvesting Performance of a Novel Nonlinear Quad-Stable Piezoelectric Energy Harvester with Only One External Magnet. *Machines* 2022;10:803. <https://doi.org/10.3390/machines10090803>.
- [65] Dhote S, Li H, Yang Z. Multi-frequency responses of compliant orthoplanar spring designs for widening the bandwidth of piezoelectric energy harvesters. *Int J Mech Sci* 2019;157–158:684–91. <https://doi.org/10.1016/j.ijmecsci.2019.04.029>.
- [66] Chen K, Fang S, Gao Q, Zou D, Cao J, Liao W-H. An enhanced nonlinear piezoelectric energy harvester with multiple rotating square unit cells. *Mech Syst Signal Process* 2022;173:109065. <https://doi.org/10.1016/j.ymssp.2022.109065>.
- [67] Forsberg G, Geréb G, Bjurström J, Rusu C, Lundgren P, Tiedke S. Piezoelectric Energy Harvesting For Rotating System. 19th International Conference on Micro and Nanotechnology for Power Generation and Energy Conversion Applications, PowerMEMS, Kraków: 2019.
- [68] Wang Q, Zhang Y, Sun NX, McDaniel JG, Wang ML. High power density energy harvester with high permeability magnetic material embedded in a rotating wheel. In: Gyekenyesi AL, editor., 2012, p. 83470V. <https://doi.org/10.1117/12.916980>.
- [69] Li M, Wen Y, Li P, Yang J, Dai X. A rotation energy harvester employing cantilever beam and magnetostrictive/piezoelectric laminate transducer. *Sens Actuators A Phys* 2011;166:102–10. <https://doi.org/10.1016/j.sna.2010.12.026>.
- [70] Gu L, Livermore C. Passive self-tuning energy harvester for extracting energy from rotational motion. *Appl Phys Lett* 2010;97:081904. <https://doi.org/10.1063/1.3481689>.
- [71] Zhang Y, Zheng R, Kaizuka T, Su D, Nakano K, Cartmell MP. Broadband vibration energy harvesting by application of stochastic resonance from rotational environments. *Eur Phys J Spec Top* 2015;224:2687–701. <https://doi.org/10.1140/epjst/e2015-02583-7>.
- [72] Kim H, Zuo L, Tai W che. Self-tuning stochastic resonance energy harvester for smart tires. In: Erturk A, editor. *Active and Passive Smart Structures and Integrated Systems XII*, SPIE; 2018, p. 29. <https://doi.org/10.1117/12.2296689>.
- [73] Kim H, Tai WC, Parker J, Zuo L. Self-tuning stochastic resonance energy harvesting for rotating systems under modulated noise and its application to smart tires. *Mech Syst Signal Process* 2019;122:769–85. <https://doi.org/10.1016/j.ymssp.2018.12.040>.
- [74] V. Experimental researches in electricity. *Philos Trans R Soc Lond* 1832;122:125–62. <https://doi.org/10.1098/rstl.1832.0006>.
- [75] Hampshire DP. A derivation of Maxwell's equations using the Heaviside notation. *Philosophical Transactions of the Royal Society A: Mathematical, Physical and Engineering Sciences* 2018;376:20170447. <https://doi.org/10.1098/rsta.2017.0447>.

- [76] Derby N, Olbert S. Cylindrical magnets and ideal solenoids. *Am J Phys* 2010;78:229–35. <https://doi.org/10.1119/1.3256157>.
- [77] Camacho JM, Sosa V. Alternative method to calculate the magnetic field of permanent magnets with azimuthal symmetry. *Revista Mexicana de Física E* 2013;59:8–17.
- [78] Bird JO, Chivers PJ. Electromagnetism and magnetic circuits. *Newnes Engineering and Physical Science Pocket Book*, Elsevier; 1993, p. 77–87. <https://doi.org/10.1016/B978-0-7506-1683-6.50013-8>.
- [79] Say M, Eastham J. Motors and Actuators. *Electrical Engineer's Reference Book*, Elsevier; 2003, p. 20-1-20–44. <https://doi.org/10.1016/B978-075064637-6/50020-4>.
- [80] Li Z, Liu Y, Yin P, Peng Y, Luo J, Xie S, et al. Constituting abrupt magnetic flux density change for power density improvement in electromagnetic energy harvesting. *Int J Mech Sci* 2021;198:106363. <https://doi.org/10.1016/j.ijmecsci.2021.106363>.
- [81] Amjadian M, Agrawal AnilK, Nassif HH. Development of An Analytical Method for Design of Electromagnetic Energy Harvesters with Planar Magnetic Arrays. *Energies (Basel)* 2022;15:3540. <https://doi.org/10.3390/en15103540>.
- [82] Ordoñez V, Arcos R, Romeu J. A high-performance electromagnetic vibration energy harvester based on ring magnets with Halbach configuration. *Energy Conversion and Management: X* 2022;16:100280. <https://doi.org/10.1016/j.ecmx.2022.100280>.
- [83] Carneiro P, Soares dos Santos MP, Rodrigues A, Ferreira JAF, Simões JAO, Marques AT, et al. Electromagnetic energy harvesting using magnetic levitation architectures: A review. *Appl Energy* 2020;260:114191. <https://doi.org/10.1016/j.apenergy.2019.114191>.
- [84] Cai M, Liao W-H. Enhanced electromagnetic wrist-worn energy harvester using repulsive magnetic spring. *Mech Syst Signal Process* 2021;150:107251. <https://doi.org/10.1016/j.ymssp.2020.107251>.
- [85] Xu J, Leng Y, Sun F, Su X, Chen X. Modeling and performance evaluation of a bi-stable electromagnetic energy harvester with tri-magnet levitation structure. *Sens Actuators A Phys* 2022;346:113828. <https://doi.org/10.1016/j.sna.2022.113828>.
- [86] Foong FM, Thein CK, Yurchenko D. Structural optimisation through material selections for multi-cantilevered vibration electromagnetic energy harvesters. *Mech Syst Signal Process* 2022;162:108044. <https://doi.org/10.1016/j.ymssp.2021.108044>.
- [87] Jiles DC, Atherton DL. Theory of ferromagnetic hysteresis. *J Magn Magn Mater* 1986;61:48–60. [https://doi.org/10.1016/0304-8853\(86\)90066-1](https://doi.org/10.1016/0304-8853(86)90066-1).
- [88] Jiles DC, Atherton DL. Theory of ferromagnetic hysteresis (invited). *J Appl Phys* 1984;55. <https://doi.org/10.1063/1.333582>.

- [89] Elishakoff I. Who developed the so-called Timoshenko beam theory? *Mathematics and Mechanics of Solids* 2020;25:97–116.
<https://doi.org/10.1177/1081286519856931>.
- [90] Timoshenko S. *History of Strength of Materials: With a Brief Account of the History of Theory of Elasticity and Theory of Structures*. Dover Publications; 1983.
- [91] Euler L, Daudet R, Delamonce FPJ, Dibner B. *Methodus inveniendi lineas curvas maximi minimive proprietate gaudentes, sive, Solutio problematis isoperimetrici latissimo sensu accepti*. Genevæ: Apud Marcum-Michaelem Bousquet & Socios; 1744.
<https://doi.org/10.5479/sil.318525.39088000877480>.
- [92] Erturk A, Inman DJ. A Distributed Parameter Electromechanical Model for Cantilevered Piezoelectric Energy Harvesters. *J Vib Acoust* 2008;130.
<https://doi.org/10.1115/1.2890402>.
- [93] Erturk A, Inman DJ. On Mechanical Modeling of Cantilevered Piezoelectric Vibration Energy Harvesters. *J Intell Mater Syst Struct* 2008;19:1311–25.
<https://doi.org/10.1177/1045389X07085639>.
- [94] Liao Y, Sodano H. Optimal power, power limit and damping of vibration based piezoelectric power harvesters. *Smart Mater Struct* 2018;27:075057.
<https://doi.org/10.1088/1361-665X/aabf4a>.